University of Mohamed Kheider of Biskra

Exact Sciences and Sciences of Nature and Life

Matter Sciences

Final Dissertation in Master

Matter Sciences

Physics

Energy Physics and Renewable Energies

Presented by:

NACEUR INTISSAR and ZERAOULIA MABROUKA

Qualitative study of Indium Gallium Nitride (InGaN) – based solar cell.

Jury:

LAZNAK SAMIRA	M.C. « A »	Med Khider University- Biskra	President
MEFTAH AMJAD	Professor	Med Khider University- Biskra	Supervisor
BOUHDJAR ABDLFODHIL	M.C. « B»	Med Khider University- Biskra	Examiner

Academic Year:**2018/2019**

بسم الله الرحمن الرحيم

Acknowledgements

First, I thank Allah the completely powerful for having agreed his infinite kindness, courage, the force and patience to complete this modest work.

After that, I make a point of profoundly thanking to my supervisor Miss Meftah Amjad for his help, support, guidance and encouragement. She has been a great support on all fronts and made my master dissertation journey a memorable experience. I could not have imagined having a better advisor and mentor for my Master study.

I am very grateful to the members of the jury: Doctor Laznak Samira and Doctor Bouhdjar Abdlfodhil for accepting to judge this thesis.

We also offer thanks to the PhD student who helped us and wish her success in her scientific path and that Allah preserves her.

Dedication

To our support in life…

To those who taught us tender without waiting…

To whom we carry Their names with pride…

I hope of god to extend their age to see the fruits come harvest after long waiting…

And your words will remain stars that I will guide today, tomorrow and forever…

Our fathers

To the one who gave us love and affection…

To the source of The tenderness and the secret of existence…

To whom was Their prayer the secret of us success…

Our mothers.

LIST OF FIGURES

LIST OF TABLES

TABLE OF CONTENTS

General introduction

General introduction

The importance of energy in our society has become evident in the last few years. Among the different alternative energies, solar energy has the very desirable property of being essentially unlimited and of being neither polluting nor physically dangerous [1]. It is the source of life. An amazing resource radiates energy and provides us with heat and light by incorporating hydrogen into helium in essence. We call this solar radiation. Only about half of this solar radiation makes it reach the Earth's surface. The rest is absorbed or reflected in clouds and the atmosphere. However, we receive sufficient energy from the sun to meet the energy requirements of all mankind - millions of times. Solar energy - energy from the sun - is a vast, inexhaustible and clean resource.

Sunlight, or solar energy, can be used directly for heating and lighting homes and businesses, for generating electricity, and for hot water heating, solar cooling, and a variety of other commercial and industrial uses. Most critical, given the growing concern over climate change, is the fact that solar electricity generation represents a clean alternative to electricity from fossil fuels, with no air and water pollution, no global warming pollution, no risks of electricity price spikes, and no threats to our public health [2].

Today, solar cells are highlighted, which are electronic devices that convert solar energy into electrical energy. There are several types of solar cells based on different semiconductor materials for example: Indium Gallium Selenide ($CIGS$), Gallium Arsenide($GaAs$), silicon (Si)...etc. In our work, we will investigate the indium gallium nitride ($InGaN$)-based solar cells. The $InGaN$ solar cells promise a theoretical conversion efficiency relatively higher than traditional Si based solar cells [3]. The $InGaN$ material system offers a substantial potential to develop ultra-high efficiency solar cells. It has a wide band gap ranging from [0.7-3.4 eV]. Most uses of these solar cells are in space applications.

However, efficiency of experimental $InGaN$ solar cells is lower than expected. The theoretical maximum solar cell efficiency limit for a single junction has been shown to be 33.5 % [4] but the experimental efficiency closer to reality is less **.**

Based on the above, our study will focus on the quantitative study of Indium Gallium Nitride

($InGaN$) based solar cells, by simulation using Silvaco-Atlas software. The manuscript is consisting of a general introduction and conclusion, in addition to four chapters organized as follows:

❖   The first chapter presents an overview on the solar cells including their principle, electrical characteristics, operation mode and a comparison between some examples of the solar cells.

❖   The second chapter is devoted to the Indium Gallium Nitride ($InGaN$) alloy properties and concepts as a promising material for solar cells.

❖   The third chapter is a simple exhibition of the Silvaco- Atlas simulation software, and its implementation as part of our work.

❖   The fourth chapter presents the main part of our work on the investigation of $InGaN$ based solar cells, with discussion and comments on the major results obtained from our study.
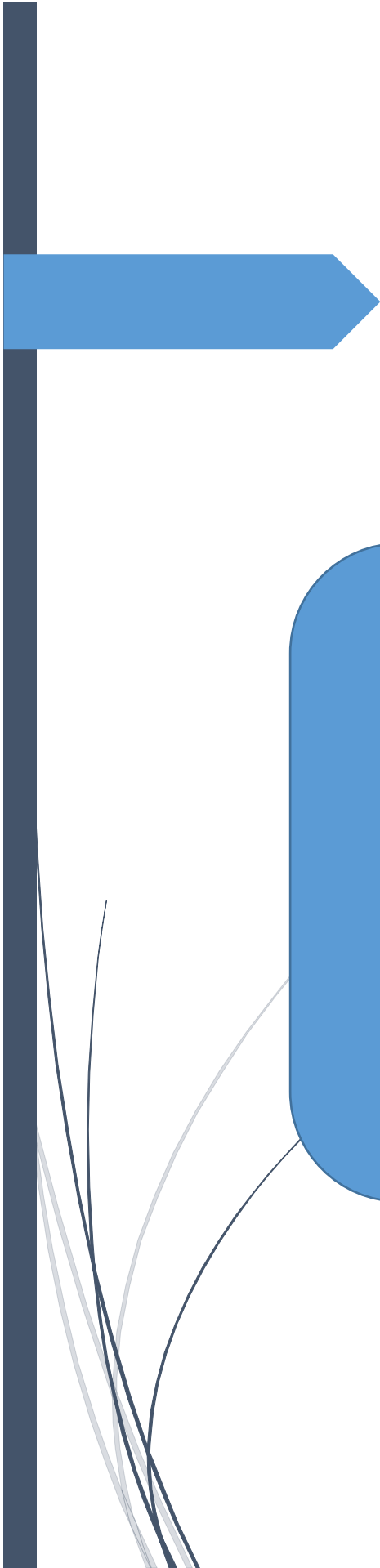
Chapter I:

Solar cells- an overview.

I.1 Introduction

Each year, Earth receives a huge amount of solar energy. In order to use, we must Change it to another format that can be used by our devices, for example, electricity (photovoltaic solar energy)[5]. Earth receives an incredible supply of solar energy

The sun that is an intermediate star is a fusion reactor burn more than 4 billion years. It provides sufficient energy in One minute to provide the world's energy needs for one year. In fact, "the amount of solar radiation hit the earth over a three-day period is equivalent to energy stored in all fossil energy sources." [6]. solar energy becomes the earth's major renewable energy resource, and the exploitation of the energy from the sun is the potential key to a sustainable energy production in future, where solar energy offers a very large amount of technical potential of over1000 EJ which is near twice the 2010 global primary energy supply of 510 EJ[7]. In this chapter, we give an overview of some concepts related to solar cells.

I.2 History of solar cell

The solar cell industry has been so small that the first ban on Arab oil has been imposed in 1973. Until then, the solar cell industry established a foothold Low level but steady cell production and range and performance [8]**.** How the history of solar cells began and how they evolved?

In 1839 Alexander Edmund Beckerle noted Photovoltaic (PV) effect by an electrode in a light conductive solution. It is useful to look at the history of photovoltaic cells since that time there are lessons to be learned which could provide guidance for future development Photovoltaic cells. Table I.1 Gives developments during the time domain from $[1839 - 1904]$, and the table I.2 summarizes the events between 1950 and 1954 [9]. Since we will talk about the solar cells$InGaN$, we have to mention a small piece about them. It was first dealt with GaN in 1969 by setting it up for optical and electrical characterization. This was done by Maruska and Tietjen[8]. After a good discovery of its characteristic and band gap $E_g = 3.39ev$, Adding the indium (In_x) element to the $Ga_{1-x}N$ led to the opening of the band gap $(0.4 - 3.4)$ eV**.**

Table I. 1: [1839-1904] Years of Discovery [4].

1839	Alexandre Edmond Becquerel observes the photovoltaic effect via an electrode in a conductive solution exposed to light.
1877	W.G. Adams and R.E. They observed the photovoltaic effect in solidified selenium and published a paper on the selenium cell. 'The action of light on selenium', in''Proceedings of the Royal Society''.
1883	Charles Fritts develops a solar cell using selenium on a thin layer of gold to form a device giving less than 1 % efficiency.
1904	Wilhelm Hallwachs makes a semiconductor-junction solar cell (copper and copper oxide).

Table I. 2: [1950-1954] Events of the years [4].

1950	Bell labs produce solar cells for space activities.
1953	1953—Gerald Pearson begins research into lithium-silicon photovoltaic cells.
1954	Bell labs announce the invention of the first modern silicon solar cell. These cells have about 6 % efficiency.

I.3 What do we mean by the solar cell?

Photovoltaics is the field of technology and research related to the devices, which directly convert sunlight into electricity. It is the elementary building block of the photovoltaic technology. In addition, they are made from semiconductors materials. We can also provide a simple definition of the solar cell; A PV solar cell is a device that converts energy directly electromagnetic (solar radiation) in direct electrical energy directly usable (Figure I.1) [10, 11]**.**
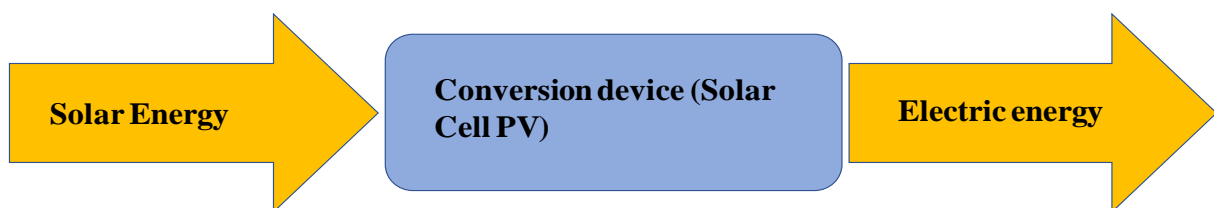
Figure I. 1: Transform solar energy into electric energy by the solar cell [11]

I.4 Solar spectrum

The solar spectrum changes throughout the day and with the location. Standard reference spectra are defined to allow the performance comparison of photovoltaic devices from different manufacturers and research laboratories. The standard spectra were refined in the early 2000s to increase the resolution and to coordinate the standards internationally. The previous solar spectrum, ASTMG159, was withdrawn from use in 2005. In most cases, the difference between the spectrum has little effect on device performance and the newer spectra are easier to use[12]. The spectrum outside the atmosphere, the 5,800 K black body, is referred to as "AM_0", meaning, "zero atmospheres". Cells used for space power applications, like those on communications satellites are generally characterized using AM_0.

The spectrum after traveling through the atmosphere to sea level with the sun directly overhead is referred to as "AM_1". This means "one atmosphere"[13]. A typical solar spectrum, as a plot of spectral irradiance vs wavelength, is shown in figure I.2.
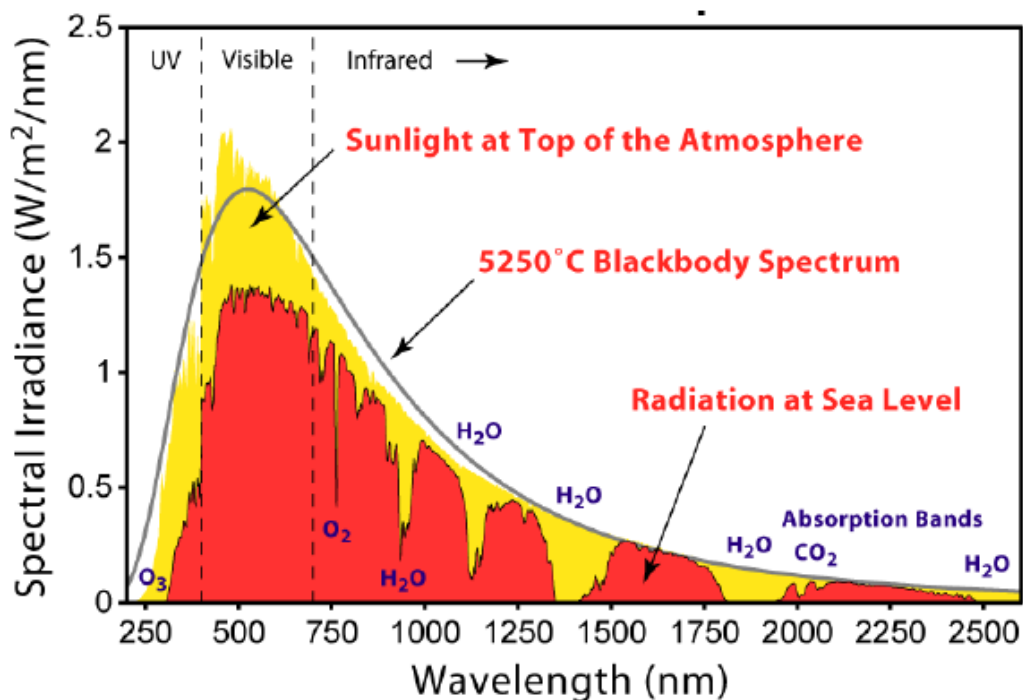
Figure I. 2: Typical solar spectrum at the top of the atmosphere and at sea level. The difference is the radiation absorbed/scattered by the atmosphere. The spectrum of a black body at 5250 C is also superimposed and used for modeling. [13]

I.5 The air mass

The Air Mass is the path length which light takes through the atmosphere normalized to the shortest possible path length (that is, when the sun is directly overhead). The Air Mass quantifies the reduction in the power of light as it passes through the atmosphere and is absorbed by air and dust. The Air Mass is defined by:

$$AM = \frac{1}{\cos{(\theta)}} = \sqrt{\frac{h^2+s^2}{h^2}} = \sqrt{1 + \frac{s^2}{h^2}}$$ (I.1)

Where θ is the angle from the vertical (zenith angle). When the sun is directly overhead, the Air Mass is one [13].
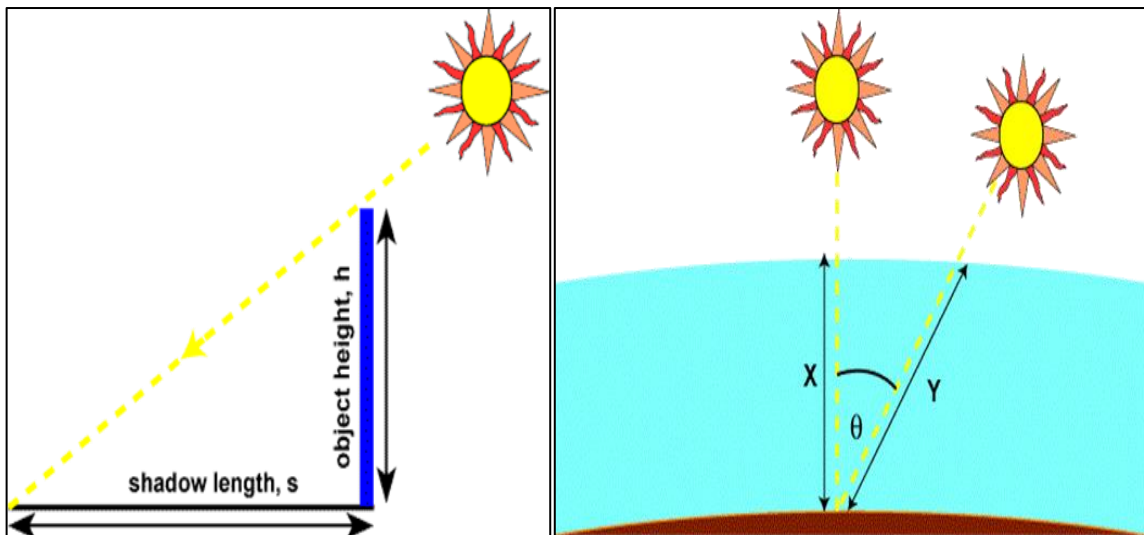
Figure I. 3: The air mass represents the proportion of atmosphere that the light must pass through before striking the earth relative to its overhead path length, and is equal to Y/X.

The standard spectrum at the ground level is called $AM1.5G$ (G means the total consisting of the direct and scattered vehicle) or $AM1.5D$ (which contains the direct vehicle only). Generally approximates to 1 kW/m^2.
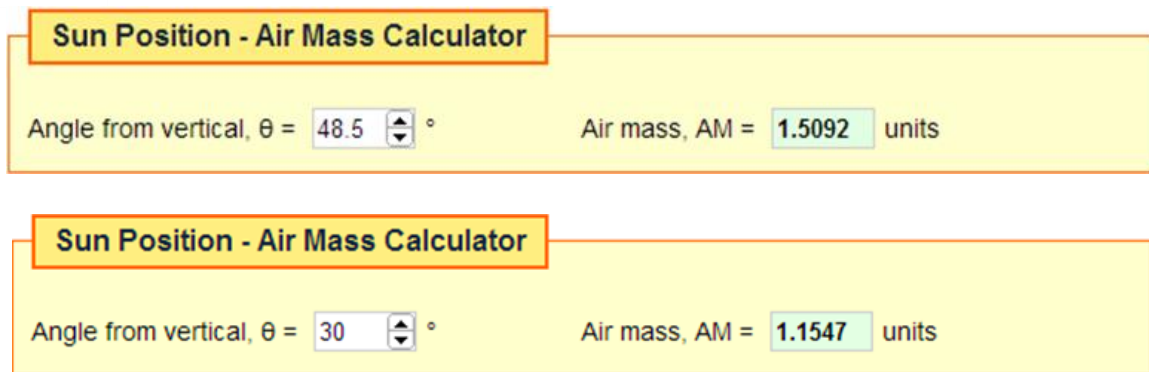
Figure I. 4: A model showing the effect of air mass on the solar spectrum in the PV Lighthouse Solar Spectrum Calculator[12].

The solar spectrum outside the solar envelope is called AM0 because there is no atmosphere that is traversed by solar radiation. This spectrum is used to predict the performance of solar cells in space.

I.6 Solar cell work

The solar cell is an electronic compound that converts sunlight directly into electricity. The bright light on the cell produces both current and voltage to generate electrical power. This first requires a light-absorbing material that can transfer the electron to a higher energy level and secondly move this electron from the cell to an external circuit. This electron then expels its energy in the outer circuit and returns to the cell. Semi-conveyors in the form of a p-n junction carried out virtually all solar transformations.
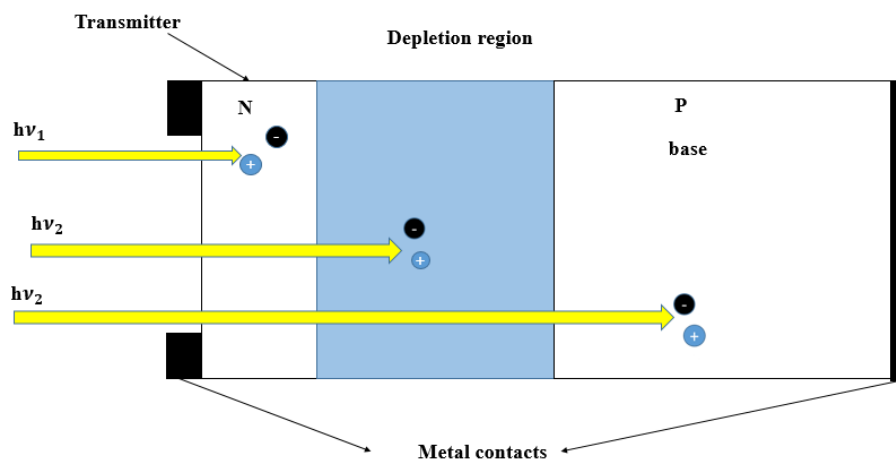
Figure I. 5: Structure of a photovoltaic cell. The respective dimensions of the different zones are not respected [14].

Incident photons create carriers in areas N and P and in the zone of space charge. Photo-carriers will behave differently depending on the region:

❖ In zone N or P, the minority carriers who reach the zone of space charge are "sent" by the electric field in the p area (for holes) or in zone n (for electrons) where they will be the majority. We will have a diffusion photocurrent.

❖ In the space charge area, the electron/hole pairs created by the incident photons are dissociated by the electric field: his electrons will go to region n, the holes to the region p. we will have a photocurrent generation.

These tow contributions are added to give a resulting photocurrent I_{ph}. It is a current of minority carriers. It is proportional to the light intensity [14].

I.7 Pin diode solar cells

The pin diode is a device that has a structure with three distinct layers: a heavily doped thin p^+-type layer, a relatively thick intrinsic (i) layer, and a heavily doped thin n^+-type layer, as shown in the figure I.6. When the structure is first formed, holes diffuse from the p^+-side and electrons from the n^+-side into the i layer where they recombine and disappear. This leaves behind a thin layer of exposed negatively charged acceptor ions in the p^+-side and a thin layer of exposed positively charged donor ions in the n^+-side. The two charges are separated by the I layer of thickness W. There is a uniform built in the field E_0 in the i layer from the exposed positive ions to the exposed negative ions, since there is no net space charge in the i layer, from:

$$\frac{dE}{dx} = \frac{\rho}{\varepsilon_0 \varepsilon_r} = 0 \qquad\qquad\qquad \textbf{(I.2)}$$

The field must be uniform, in contrast, the built −in field in the depletion layer of a pn junction is not uniform [15].
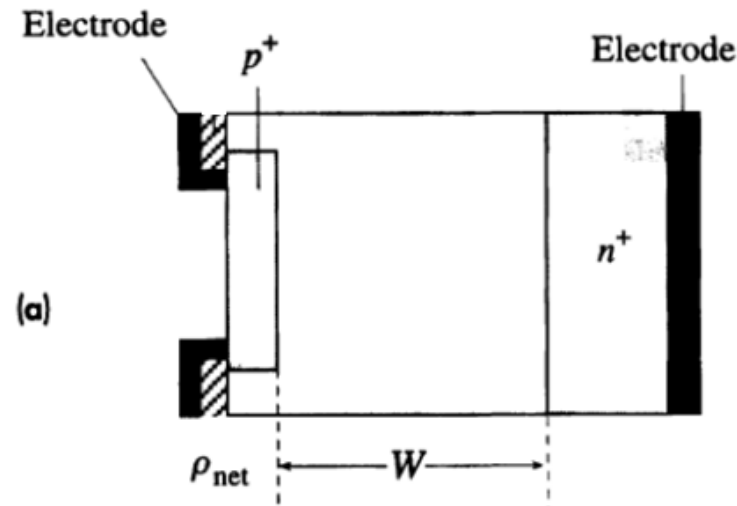
Figure I. 6: The schematic structure of an idealized pin photodiode[15].

I.8 Solar cell parameters

The main characteristic quantities of solar cells are:

- Short circuit current I_{SC}
- Open circuit voltage V_{OC}
- The fill factor FF
- Energy conversion efficiency η
- The spectral response R_S

I.8.1 Short circuit current I_{SC}

The short-circuit current expressed in mA is the current flowing in the cell under illumination and by shorting the terminals of the cell. It grows linearly with the illumination intensity of the cell and it depends on the illuminated surface, the wavelength of the radiation, the mobility of the charge carriers and the temperature. It can also be said that the current is the current initiated by the cell under illumination in reduce output. Which means:

$I_{SC} = I(V = 0)$ and equations analytical:

$$I = I_{ph} - I_{SC}(e^{V/V_T} - 1) \tag{I.3}$$
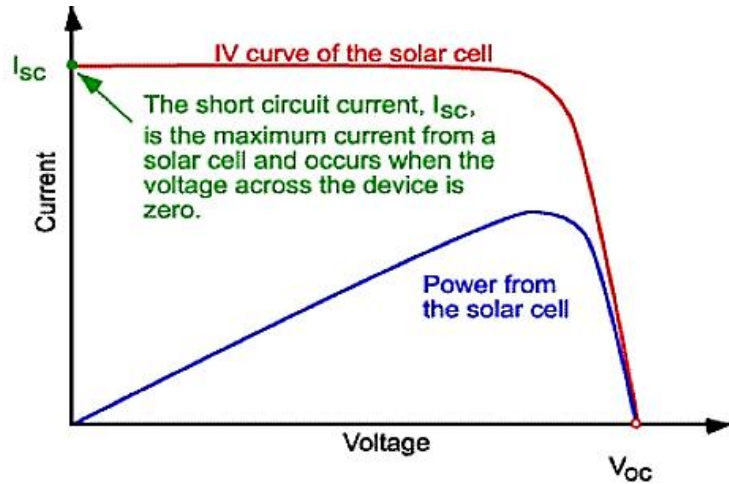
Figure I. 7: The short circuit current I_{SC} [12].

I.8.2 Open circuit voltage V_{OC}

The open circuit voltage V_{OC} is the maximum voltage available from a solar cell, and this occurs at zero current. The open circuit voltage expresses the direct polarization of the resulting cell by polarizing the junction with the light -generated current. The schematic of the open circuit voltage on the I-V curve is in figure I.9.

$$I_0 \left(e^{\frac{eV_{OC}}{\eta k_b T}} - 1 \right) - I_{SC} = 0 \tag{I.4}$$

$$V_{OC} = \frac{\eta . K_b . T}{e} ln \left(\frac{I_{SC}}{I_0} - 1 \right) \tag{I.5}$$
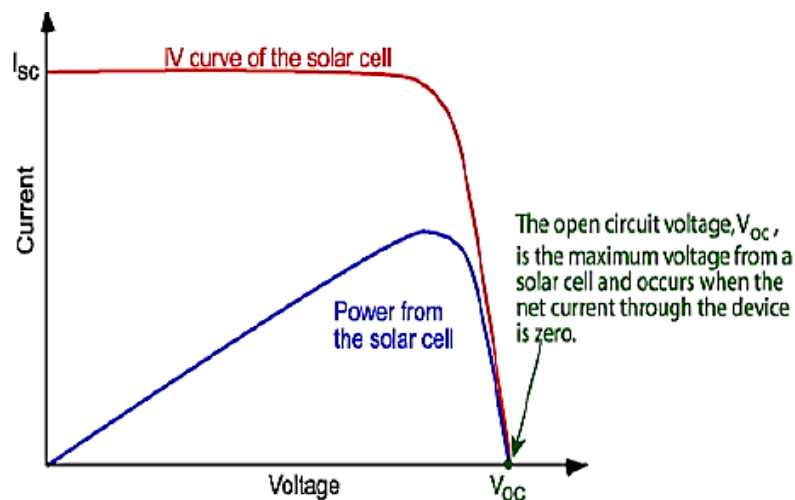
Figure I. 8 : The open circuit voltage V_{OC} [12]**.**

I.8.3 The fill factor FF

The "fill factor" is the ratio of maximum power P_m, to the open-circuit V_{oc} voltage and short circuits current I_{SC}. It is known by the abbreviation "FF".[2] the FF is illustrated in figure I.9.

$$FF = \frac{I_m V_m}{V_{oc} I_m} = \frac{P_m}{V_{oc} I_{sc}} \tag{I.6}$$

In the ideal case, the fill factor (FF) is 100 %. For a silicon solar cell, the FF typically ranges between 77.0% and 82.0%.
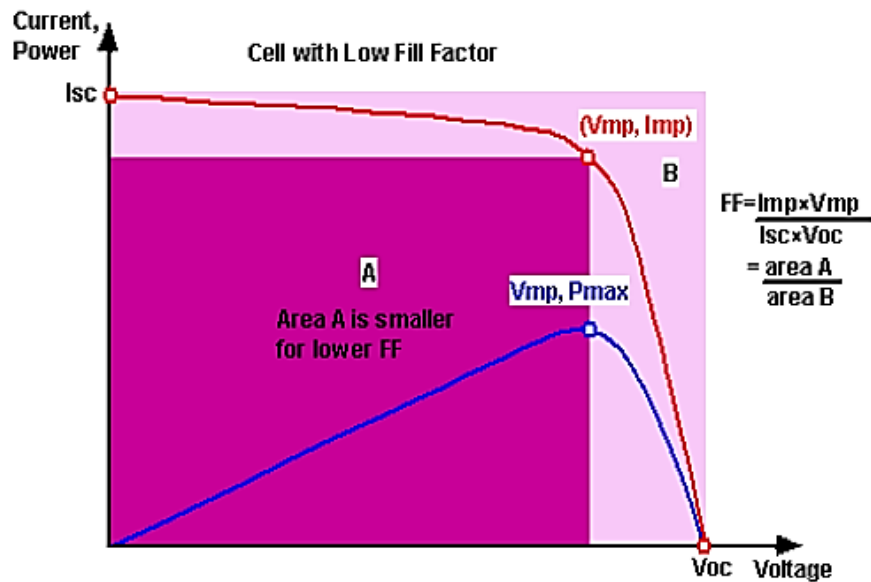
Figure I. 9: The fill factor FF[12].

I.8.4 Energy conversion efficiency η

Conversion efficiency is the most commonly used medium or benchmark for comparing a solar cell to another. The efficiency represents the ratio between the electrical capacity generated by the cell and the photovoltaic power it receives. Therefore, it depends on the intensity of incoming light and the temperature of the solar cell. Therefore, the conditions under which cell efficiency is measured to compare a cell to another must be controlled. In general, solar cell efficiencies are measured at 25 ° C and AM1.5 light. In space, light is $AM0$.

$$\eta = \frac{FF.V_{OC}.I_{sc}}{P_{inc}} = \frac{P_{out}^{max}}{p_{inc}} \tag{I.7}$$

I.8.5 The spectral response R_S

Quantitative efficiency gives the ratio between the number of electrons given by the cell and the number of photons contained in it, whereas the spectral response is the ratio between the electricity generated by the cell and the optical capacity of the incoming photons. In the figure, we show an example of the silicon spectral response. The spectral response is limited to long wavelengths because half of the carrier cannot absorb photons with lower-than-band capacity. However, unlike the rectangular shape of the quantum yield curves, the spectral response decreases for short wavelengths. Why?

For these wavelengths, photons have higher energies (short wavelengths mean higher energies), so the ratio between the number of generated carriers and the power (time unit energy) decreases.

The solar cell does not use any additional power higher than the prohibited range.

The inability to use excess energies and low absorption of low energies represents significant losses in the capacity of the single-link solar cell p-n.

$$SR = \frac{\lambda.t.I}{h.c.n_{ph}} \qquad \qquad \textbf{(I.8)}$$

$$SR = \frac{q\lambda}{hc}QE \qquad \qquad \textbf{(I.9)}$$
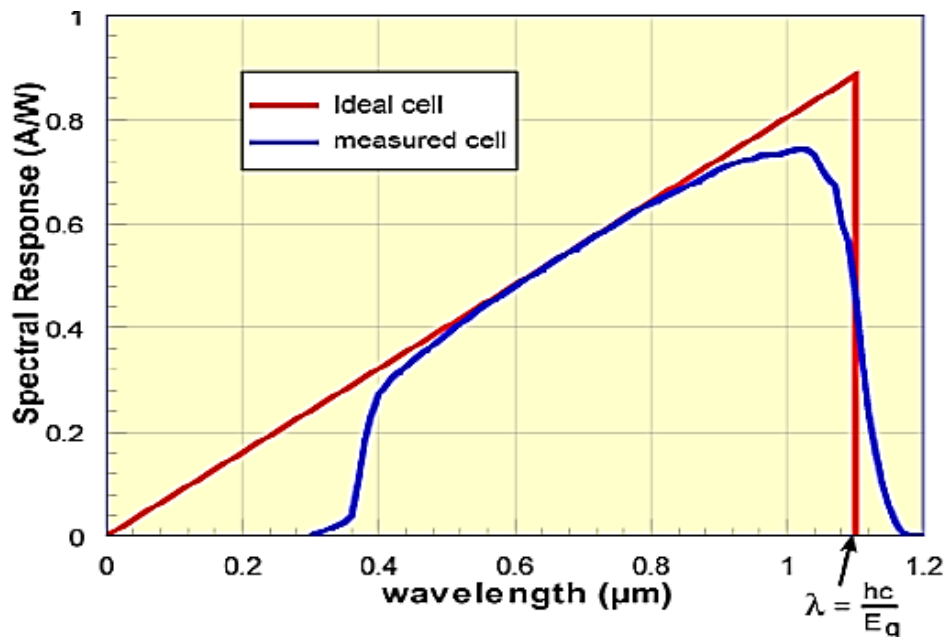
figure I. 10: Spectral response schematic [12].

I.9 Examples of solar cells

The efficiency is the most commonly used parameter to compare the performance of one solar cell to another. Efficiency is defined as the ratio of energy output from the solar cell to input energy from the sun. In addition to reflecting the performance of the solar cell itself, the efficiency depends on the spectrum and intensity of the incident sunlight and the temperature of the solar cell [16]. In a table I.3, we give some examples of solar cells based on silicon (Si), copper Indium Gallium Selenide ($CIGS$),Gallium Arsenide ($GaAs$) and Indium Gallium Nitride ($InGaN$) respectively.

Table I. 3: The table presents some examples of solar cells and their efficiency.

solar cells	efficiency
Si	The upper limit of silicon solar cell efficiency is 29% [17].
	Silicon solar cell laboratory is 25% [17].
	Silicon solar cell large –area commercial is 24%[17].
(CIGS)	Continuous research and development have led to $AM_{1.5}$cell efficiencies for $CIGS$ of up to 22.6%, as certified in 2016 [18].
GaAs	In particular, a GaAs-based thin-film solar cell could be the leader of the future thin-film solar cell market because of its unrivaled high efficiency (28.8%, Alta Devices, Sunnyvale, CA, USA1)[19].
InGaN	The theoretical maximum solar cell efficiency limit for a single junction has been shown to be 33.5 % [4].
	Modeling of an $In_{0.65}Ga_{0.35}N$single-junction solar cell by Zhang et al.[4] gave a conversion efficiency of 20.284%.

I.10 Conclusion

In this chapter, we presented some of the general concepts related to the solar cells in terms of their definition, operation mode and a comparison between some of the solar cell examples based on Si ,$CIGS$, $GaAs$, and $InGaN$, respectively. These concepts allow and facilitate us to understand and grasp the second chapter, which will be paired around the $InGaN$-based solar cells.
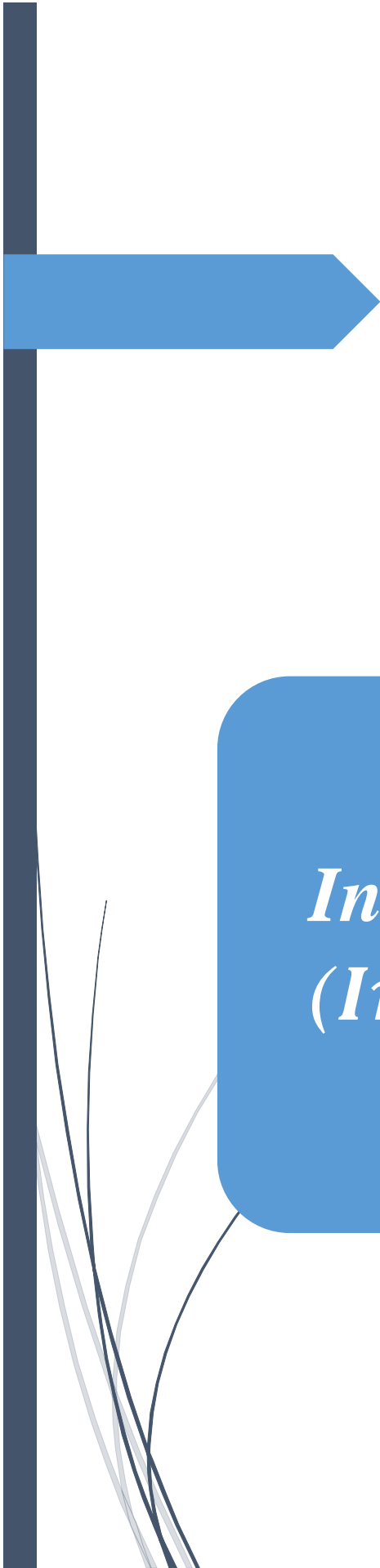
Chapter II :

Indium Gallium Nitride (InGaN) for Solar cells

II.1 Introduction

Group-III nitrides like Indium Nitride (InN), Gallium Nitride (GaN), Aluminum Nitride(AlN) and its alloys ($AlGaN$, $AlInN$, $InGaN$ and$AlInGaN$) are promising materials system for the new semiconductor devices. These nitride materials have some significant electronic and optical properties, and a tunable direct bandgaps [20]from 6.2 eV (AlN) through 3.4 eV (GaN) to 0.7 eV (InN) (figure II.1). This wide coverage of direct bandgap range from deep ultraviolet (UV) to infrared region promises a variety of applications in optoelectronics, such as light-emitting diodes (LEDs), lasers, photodetectors and solar cells. In this chapter we provide a review of Indium Gallium Nitride ($InGaN$) alloy with its advantages and difficulties for photovoltaic applications.
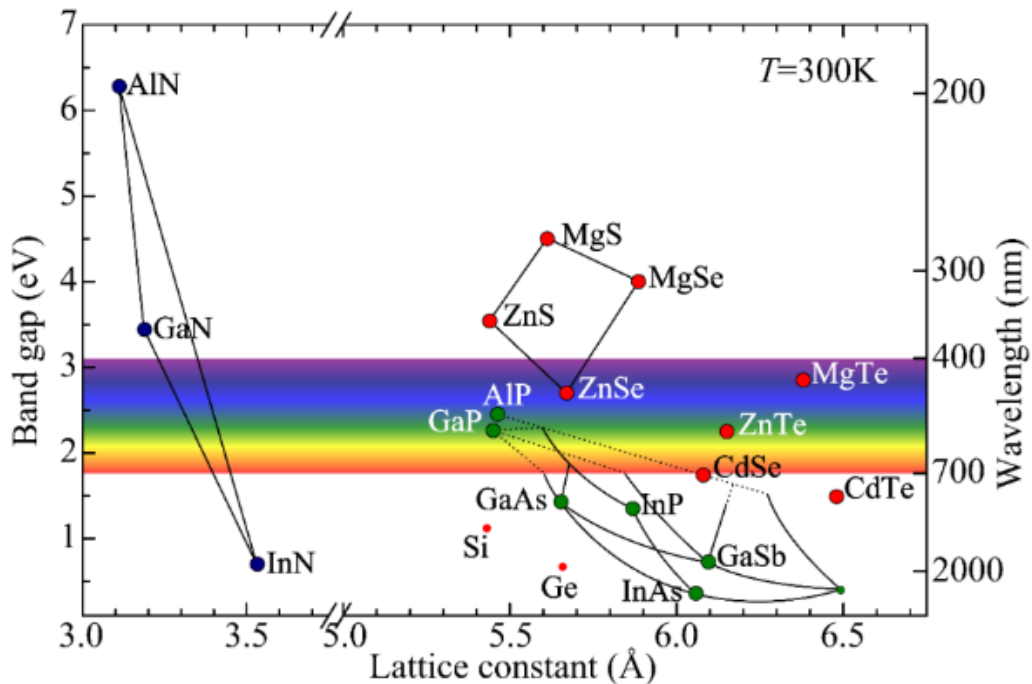
Figure II. 1: Band gap and the corresponding wavelength as a function of the lattice constant [21].

II.2 The Indium Gallium Nitride (In$_x$Ga$_{1-x}$N) Alloy
II.2.1 In$_x$Ga$_{1-x}$N: An Overview

Indium gallium nitride ($In_xGa_{1-x}N$) is a ternary III-V semiconductor alloy composed of a mixture of indium nitride (InN) and gallium nitride (GaN). The material properties of this alloy depend heavily on the ratio of indium (x) to gallium (1-x) in its composition. Most important to photovoltaic applications, by changing the material's indium content the band gap of

$In_xGa_{1-x}N$ can be tuned from 0.77 eV (InN; $x = 1$) to 3.42 eV (GaN; $x = 0$) which spans nearly the entire solar spectrum [22, 23]. Table II.1 presents the maximum theoretical efficiencies along with the calculated band gaps and compositions for each junction of an ideal $In_xGa_{1-x}N$ multi-junction solar cell [24].

Table II. 1: Junction band gaps and composition for ideal $In_xGa_{1-x}N$ multi-junction solar cells [5].

Number of Junctions	Band Gap, eV (Composition, x)				Maximum Theoretical Efficiency
	Junction 1 (Top)	Junction 2	Junction 3	Junction 4 (Bottom)	
1 (SJ)	1.12 (0.62)	-	-	-	30.57 %
2 (DJ)	1.73 (0.39)	0.93 (0.72)	-	-	40.79 %
3 (TJ)	2.02 (0.30)	1.34 (0.52)	0.71 (0.95)	-	45.08 %
4 (QJ)	2.25 (0.25)	1.7 (0.40)	1.3 (0.54)	0.73 (0.91)	48.30 %

Just like its components InN and GaN, wurtzite is the thermodynamically stable structure of In$_x$Ga$_{1-x}$N. This structure has a hexagonal close-packed lattice type with an AB atomic repeating pattern. However, under certain deposition conditions $In_xGa_{1-x}N$ can also form in the zinc-blende structure [25]. This structure has a face-centred cubic lattice type with an ABC atomic repeating pattern. The plan views of these two structures are presented in figure II.2 [24].
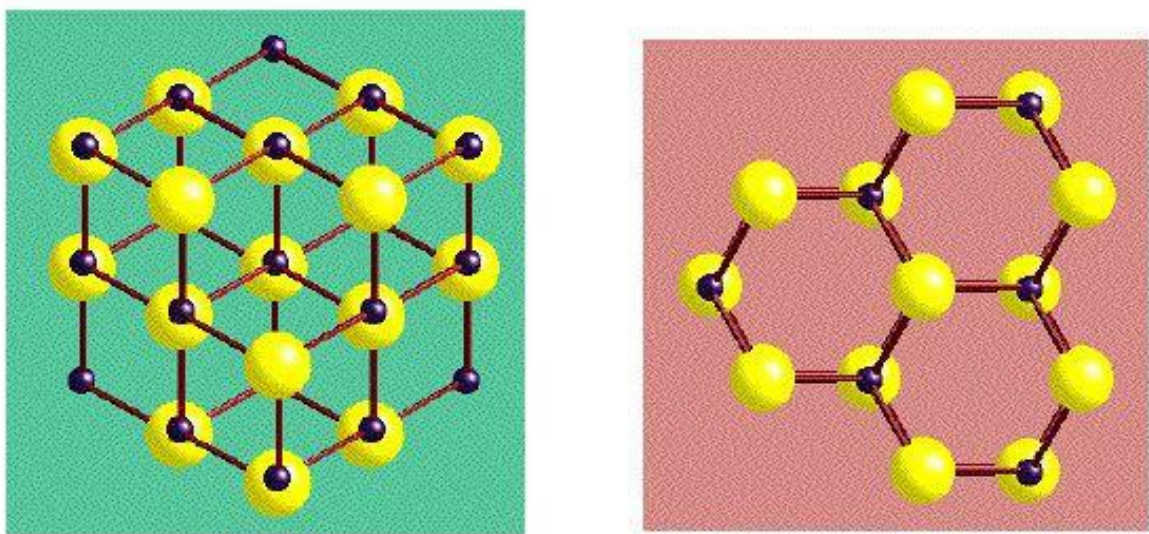
Figure II. 2: Plan views of zinc-blende (green) and wurtzite structures (pink) [24].

As a member of the III-nitride alloy semiconductor group, $In_xGa_{1-x}N$ possesses good optoelectronic properties that make it well suited for thin-film multi-junction solar cells [26]. $In_xGa_{1-x}N$ is a direct band gap semiconductor, which means that during photon absorption direct interband transitions can occur without the need of a phonon to conserve momentum [25]. Typical of direct band gap semiconductors, $In_xGa_{1-x}N$ also has a very high absorption coefficient on the order of 10^5 cm^{-1} near the band edge [27, 28]. This indicates that 99% of photons above the band gap will be absorbed in the first 500 nm of the $In_xGa_{1-x}N$ film [29]. Since only a thin layer of material is needed for efficient absorption, material costs are minimized but also the distance electrons are required to travel for extraction is kept short thus offering fewer opportunities for recombination.

As previously mentioned, the band gap of $In_xGa_{1-x}N$ can be tuned to span nearly the entire solar spectral range. This property makes $In_xGa_{1-x}N$ well-suited for multi-junction solar cells as the same alloy with different compositions can be deposited using the common metal organic chemical vapour deposition ($MOCVD$) and molecular beam epitaxy (MBE) growth processes for each layer in the device.

Other $In_xGa_{1-x}N$ properties that are beneficial for photovoltaic include a low effective mass of carriers, high carrier mobilities and high peak and saturation velocities [30, 31]. $In_xGa_{1-x}N$ is also well-suited for space applications as its high radiation resistance extends its lifetime in the UV-intense conditions [32]. Electricity generation on satellites is currently the primary use of multi-junction solar cells.

II.2.2 The band gap of In$_x$Ga$_{1-x}$N

Precise knowledge of the semiconductor's band gap (E_g) is critical for the design and fabrication of photovoltaic cells. Vegard's law, a composition-weighted relationship between band gaps at either end of the compositional range, is commonly used as an estimate for ternary materials. However, this equation produces a linear relationship between the endpoints, which does not match experimentally observed values for $In_xGa_{1-x}N$ properties. Instead, a bowing parameter (b) is added to improve accuracy. This bowing equation for the estimation of $In_xGa_{1-x}N$'s band gap is presented [33]:

$$E_g(In_xGa_{1-x}N) \ = \ x\,E_g(InN) + (1-x)E_g(GaN) - b\,x(1-x) \qquad \textbf{(II.1)}$$

The addition of the bowing parameter in Equation II.1 introduces a non-linear component (bowing effect) to the relationship. The magnitude of this bowing parameter determines the deviation from linear interpolation between the band gaps of InN andGaN. Most authors determine a bowing parameter between 1 eV and 3.8 eV (Figure II.3) with an average value of 2.17 eV [25, 27, 28, 34-37].
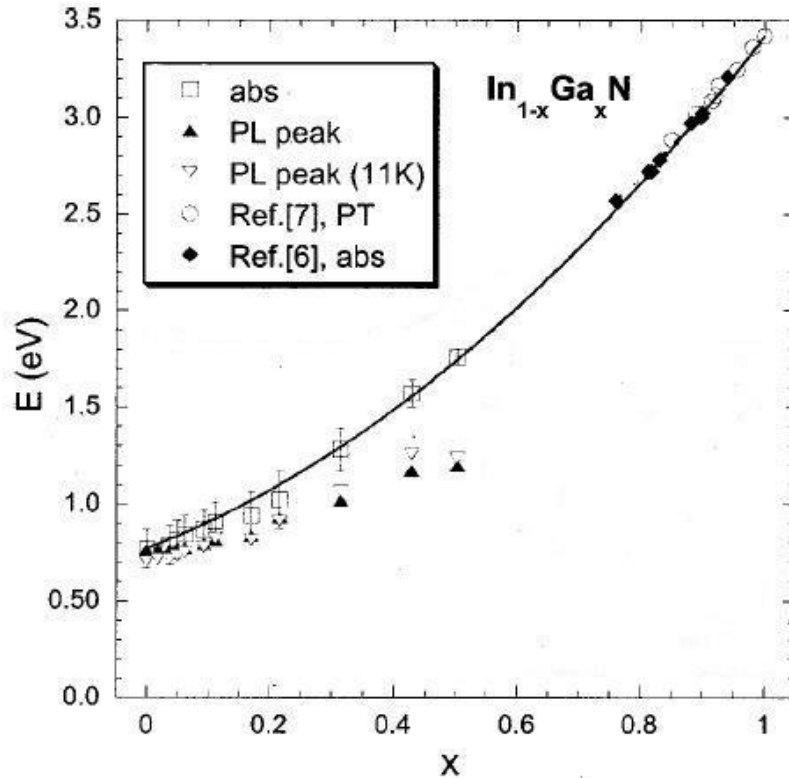
Figure II. 3: Band gap energies determined for $In_xGa_{1-x}N$ films. Solid line is the fit using a bowing parameter of 1.43 eV [36, 38, 39].

The following equation provides an approximation of Indium Gallium Nitride band gap:

$$E_g(x_{In}) = 3.42(1 - x_{In}) + 0.77x_{In} - 1.43x_{In}(1 - x_{In}) \tag{II.2}$$

Where E_G is the $InGaN$ band gap, 3.42 eV is the GaN band, 0.77 eV is the InN band gap, 1.43 eV is the bowing parameter b, x_{In} is the indium (In) concentration, and $(1 - x_{In})$ is the gallium (Ga) concentration. When plotting the band gap formula for $InGaN$ using a Matlab script, the figure II.4 is obtained[36].
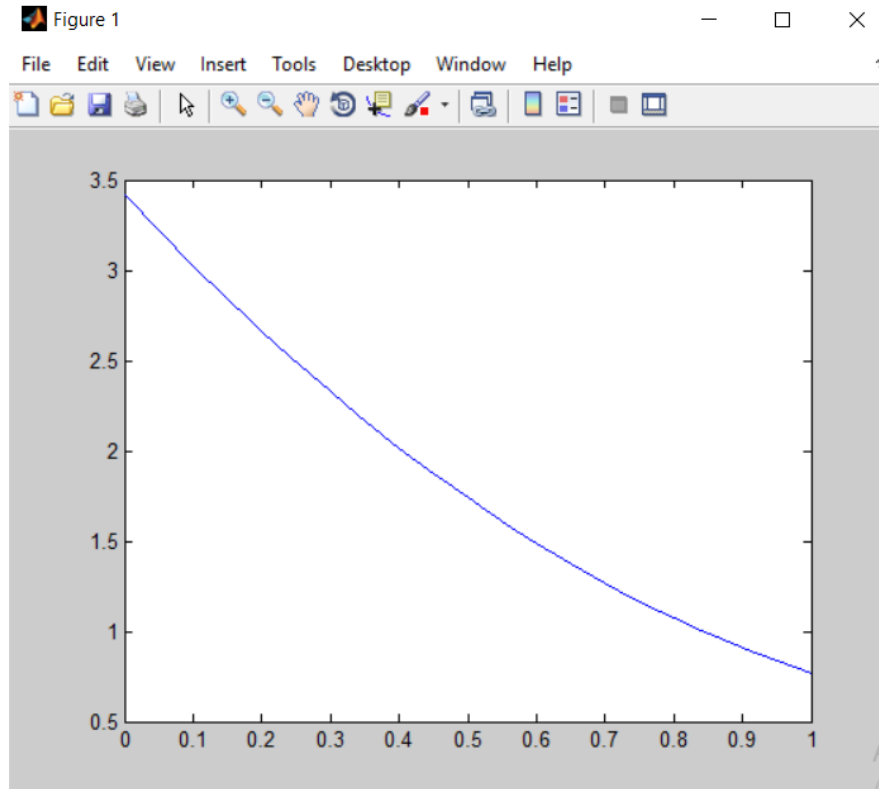
Figure II. 4: *InGaN* band gap as a function of *In* concentration (x_{In}).

The band gaps used in Silvaco Atlas simulation is calculated following the equation.II.2.

II.2.3 Absorption coefficient and refractive index of $In_xGa_{1-x}N$
II.2.3.1 Absorption coefficient

Several theoretical models have been proposed to describe the absorption coefficient $\alpha(\lambda)$ in the *InGaN* ternary alloy. Brown et al. [40] proposed the following relation to compute the absorption coefficient $\alpha(\lambda)$:

$$\alpha(\lambda) = a_0 \sqrt{a(x)\left(E - E_g\right) + b(x)(E - E_g)^2} \qquad \text{(II.3)}$$

With: $E = \dfrac{hc}{\lambda}$ $\qquad$ (II.4)

The dimensionless fitting parameters $a(x)$ and $b(x)$ are given for small indium content [40]. For more details and to consider all the indium content compositions, we use further adjustment parameters a_{fit} and b_{fit} [40]. A linear interpolation is used to find the new fitting parameters over the entire composition range. In this case, the wavelength-dependent absorption coefficient has been determined for all alloy compositions. The parameters a_{fit} and b_{fit} are given using this linear interpolation [41]:

$$a_{\text{fit}} = 12.87x^4 - 37.79x^3 + 40.43x^2 - 18.35x + 3.52 \qquad \text{(II.5)}$$

$$b_{fit} = -2.92x^2 + 4.05x - 0.66 \qquad \text{(II.6)}$$

The extinction coefficient k is related to the absorption coefficient α following the equation:

$$\alpha = \frac{4\pi}{\lambda} k \qquad \text{(II.7)}$$

Then, we can calculate the extinction coefficient k required to be added as data file in Silvaco-Atlas:

$$k = \frac{\alpha\lambda}{4\pi} \qquad \text{(II.8)}$$
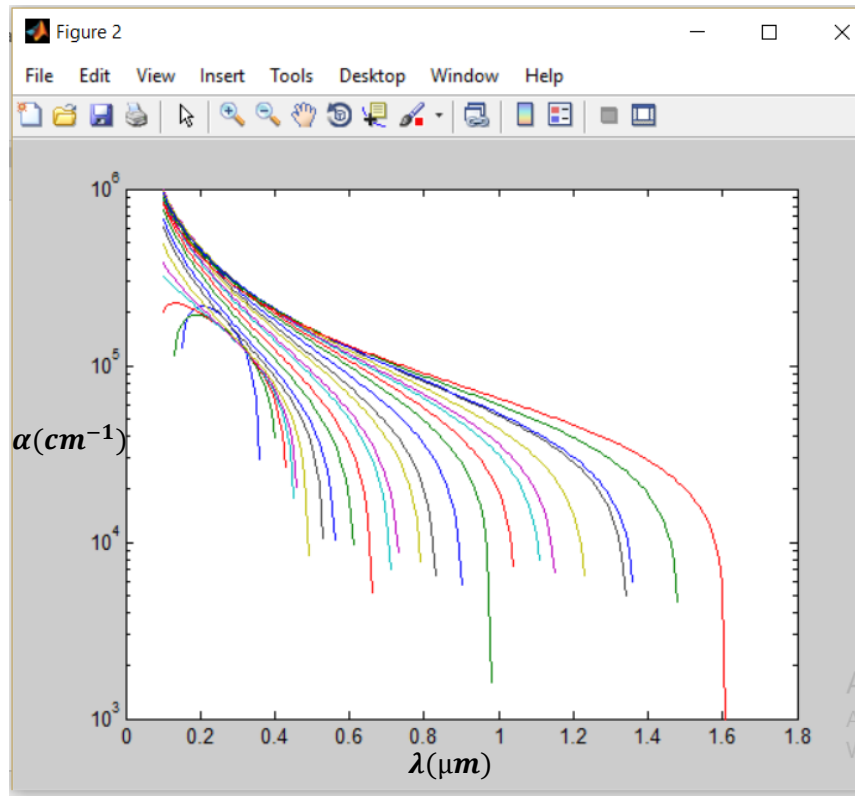
Figure II. 5: Absorption coefficient α (cm⁻¹) of *InGaN* versus wavelength ($\lambda(\mu m)$) for different *In* compositions (x_{In}) using the Matlab program and the equation (II.3).
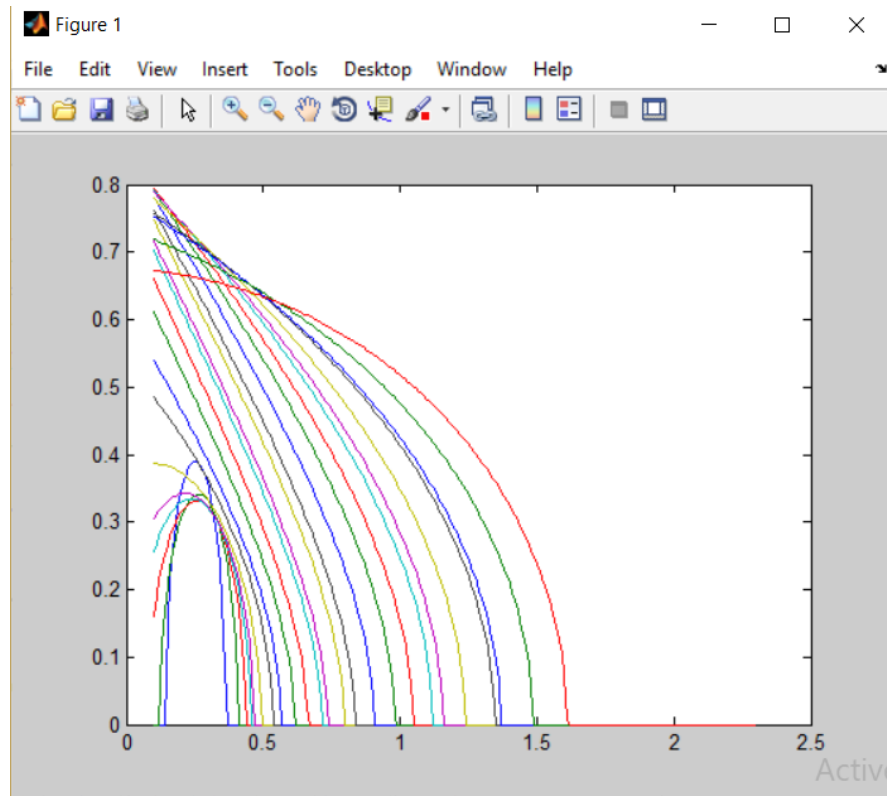
Figure II. 6: Extinction coefficient k of $InGaN$ versus wavelength ($\lambda(\mu m)$) for different In compositions (x_{In}) using the Matlab program and the equation (II.8).

II.2.3.2 Refractive index

The importance of the refractive index is due to its direct reverse proportional relation with the gap of the material and has a hyperbola profile [42]. The refractive index expresses also, the ratio between the light celerity in a vacuum and its celerity in the considered material [25]. The wavelength is also reversely proportional to the bandgap of a material in the relation:

$$E_g = \frac{1.24}{\lambda} \qquad \qquad \textbf{(II.9)}$$

Which is straight, thus the relation between the refractive index and the wavelength must be directly proportional and have the parabolic form. By interpolation one can deduce the relation n(λ), by taking some semiconductors known refractive indices and their corresponding wavelengths[25]. The results are confined in Figure II .7.
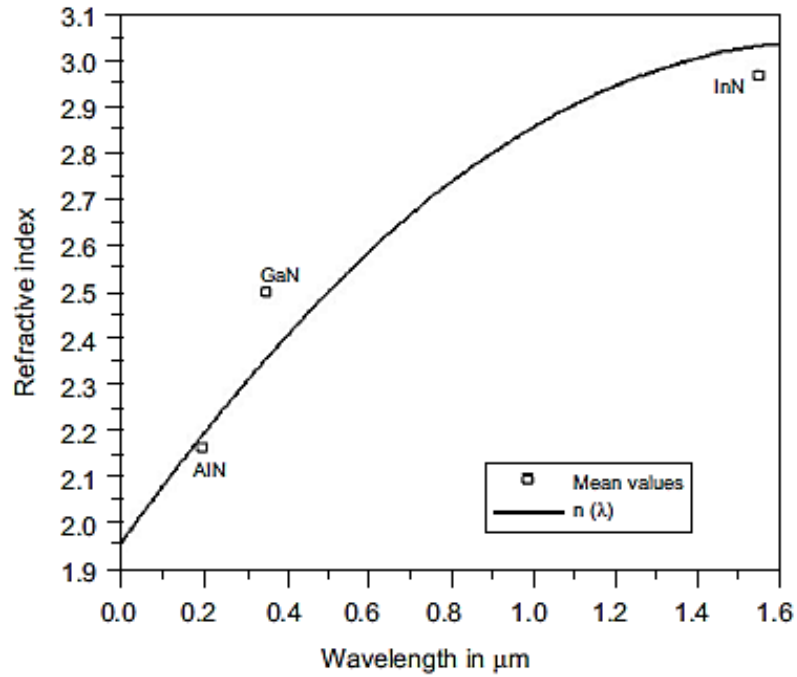
Figure II. 7: Refractive index versus wavelength in the III-Nitrides group [25].

Some assumptions allowing to calculate the refractive index of $In_xGa_{1-x}N$ using the equation (II.10):

$$n_{In_xGa_{1-x}N} = n_{InN}x + (1 - x)n_{GaN} - bx(1 - x) \qquad \textbf{(II.10)}$$
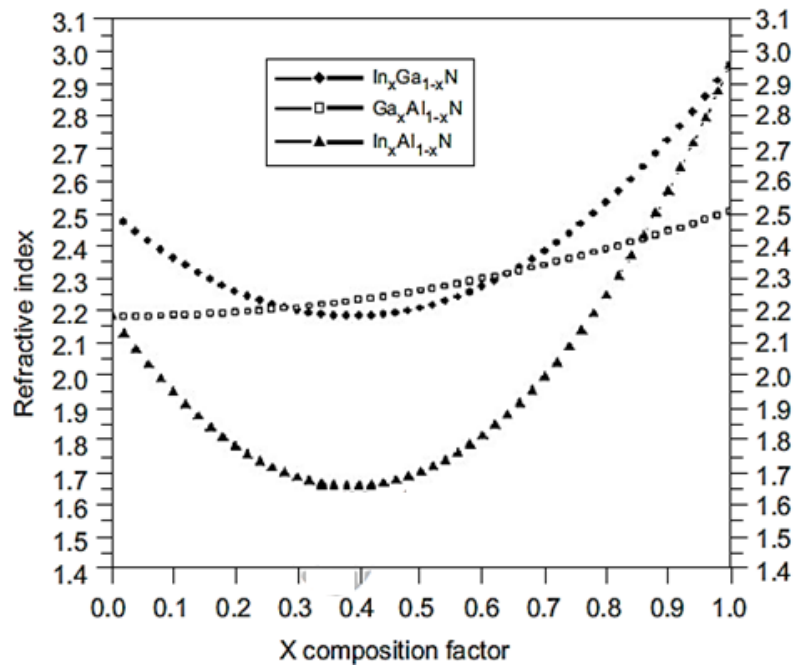
***Figure II. 8 :* Refractive index of wurtzite $In_xGa_{1-x}N, Ga_xAl_{1-x}N$ and $In_xAl_{1-x}N$**
alloys versus the molar fraction(x) [25].

In our simulations, we will use the Adachi model, which is used to calculate the refractive index of the materials and the equation that represents this model is [43]:

$$n_r(\omega) = \sqrt{A\left(\frac{\hbar\omega}{E_g}\right)^{-2}\left\{2 - \sqrt{1 + \frac{\hbar\omega}{E_g}} - \sqrt{1 - \frac{\hbar\omega}{E_g}}\right\} + B} \tag{II.11}$$

Where E_g is the bandgap, ω is the optical frequency and A and B are material composition dependent parameters. For $In_xGa_{1-x}N$, the compositional dependence of the A and B parameters are given by the expressions in Equations II.12 and II.13 respectively[43].

$$A(x) = 9.827(1 + x) - 53.57x \tag{II.12}$$

$$B(x) = 2.736(1 - x) - 9.19x \tag{II.13}$$

$II.2.4\ In_xGa_{1-x}N$ Film growth

The $In_xGa_{1-x}N$ alloys are difficult to grow in large bulk crystals due to the lack of substrate materials with closely matching lattice constants[34]. Depositing material on a substrate with a mismatched lattice constant causes the growing film to be strained (increasing strain with increasing mismatch). $In_xGa_{1-x}N$ films suffer from lattice mismatch with the most common substrates such as sapphire (GaN mismatch of 16%) and silicon (GaN and InN mismatch of 9% and 7% respectively) [24, 25] However, in addition to substrate mismatches, the growth of high-quality $In_xGa_{1-x}N$ is also hindered by lattice constant differences between InN and GaN. Various authors have placed this large mismatch at between 10 and 13% [28, 34, 44, 45].

II.2.5 Buffer layers

In order to reduce the negative effect of substrate lattice mismatch with the growing $In_xGa_{1-x}N$ films, it is common practice to use a buffer layer between the substrate and film. This layer has an intermediate lattice constant to ease the transition from substrate to film, which can reduce compressive straining during growth [34, 46]. A thin GaN buffer layer has been shown to improve the structural and optical properties of $In_xGa_{1-x}N$ films [25, 34, 35].

II.2.6 Substrate growth

II.2.6.1 Growth sapphire

The first substrate used for GaN heteroepitaxy was sapphire (Al_2O_3), by Maruskas and [35]Tietjen's in 1969, using Hybrid Vapor Phase Epitaxy (HVPE). Despite a mesh parameter and coefficient of thermal expansion far removed from those of GaN, sapphire has become its most widely used substrate. These differences cause defects in the GaN material such as dislocations, stacking defects, etc., reducing the quality of the layers. To date, the solution to overcome this problem is to deposit very thick layers (several microns) to move away from the interface. In addition, sapphire is a relatively expensive material making it impossible to use it on a large scale [47]. In addition, Sapphire substrate (Al_2O_3) is known as alpha-alumina in the purest form with no porosity or grain boundaries. A suitable combination of the chemical, mechanical, optical, surface and thermal durability properties make sapphire a preferred material for component designs especially in the field of III-Nitride technology. Sapphire is grown by different methods such as Czochralski, Kyropolus etc. [48].

II.3 Performance of Current of $In_xGa_{1-x}N$ Solar Cells

While most $In_xGa_{1-x}N$ research is conducted on improving the quality of its films, $In_xGa_{1-x}N/GaN$ solar cells have been made and tested. In addition to a high density of dislocations and other defects that increase current leakage, In_xGa_{1-x} solar cells also suffer from a difficulty in achieving both p-type doping and low-resistance Ohmic contacts .P-type doping with magnesium as an acceptor remains challenging due to the strong surface accumulation of electrons in $In_xGa_{1-x}N$ with higher indium contents. This effect can also act as a parasitic conductivity path between the contacts on $In_xGa_{1-x}N$ solar cells. Consequently, current $In_xGa_{1-x}N$ cells show less than 2% efficiency. Clearly, there is a great deal for improvement as this falls well below the potential efficiency of 48.3% for a quad-junction $In_xGa_{1-x}N$ solar cell [24] .

II.3.1 Comparison between PN and PIN

A PIN- $InGaN$ solar cell was designed and optimized with a thickness of intrinsic layer. as show in figure II.9.
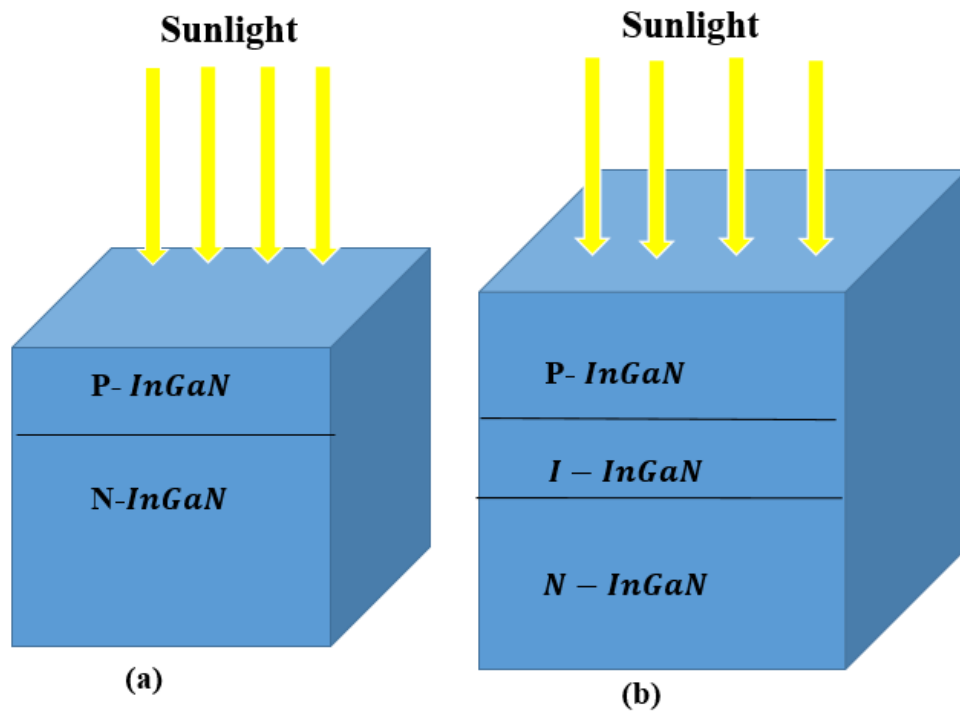
Figure II. 9: Schematic structure of a) P-N $InGaN$ Cell and b) P-I-N $InGaN$ Cell.

It is shown that the electrical parameters such as, the J_{SC} and V_{OC} has strong dependence on the thickness of I-layer[15]. Inclusion of intrinsic layer in the conventional PN structure widens the width of the depletion region as a consequence, the photo-current increases. It is also observed that the external quantum efficiency is increased with the inclusion of intrinsic layer. As compared to the PN $InGaN$ cell, the PIN cell exhibited around 2% higher efficiency [15].

The negative points in the PN link are that the width of the space delivery area does not exceed some micrometers. This means that in long wavelengths, the depth of the penetration is greater than the width of the space charge area. Most photons are absorbed outside the depletion region. There is no field for separating (electron- hole). The resulting efficiencies are relatively low in the long wavelengths. These problems are significantly mitigated in the PIN structure, where most photosynthesis occurs in the core region [49].

II.4 Conclusion

The indium gallium nitride ($In_xGa_{1-x}N$) semiconductor is a promised alloy system with a band gap that can vary continuously from ultraviolet at 3.42eV to the near infrared at 0.77eV, which matches well with the whole solar spectrum. Additionally, $InGaN$-related systems show many other favorable properties including high absorption coefficients, high carrier mobility, saturation velocities, and a superior radiation resistance. A review of this material was provided in this chapter, and research into its application for photovoltaic is still in the development stages.
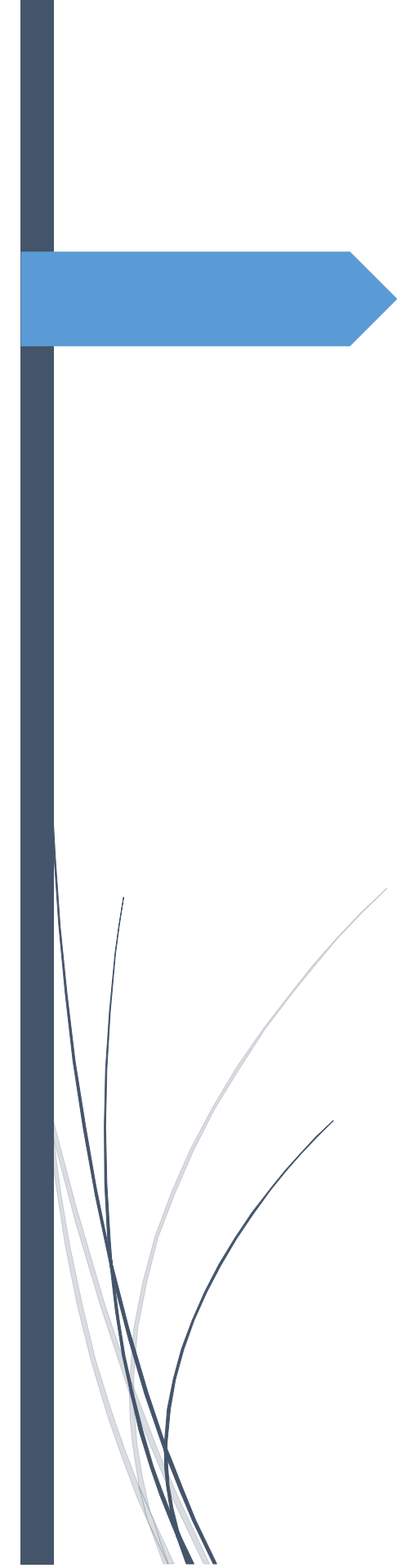
Chapter III:

Digital simulation software: Silvaco-Atlas

III.1 Introduction

By physical process simulation, we mean the use of mathematical description, or model, of a real system in the form of a computer program. This model is composed of equations that duplicate the functional relationships within the real system. A numerical method is a tool that enables the prediction of the behavior of the system from a set of parameters and initial conditions and allows us to achieve results not achievable by other means [50].

Numerical simulation is also a powerful way to analyze, predict, interpret and understand the physical phenomena governing the transport in devices such as solar cells. In addition, the study of the real behavior of solar cells requires a detailed description of the device to simulate and materials used in its realization. The selection of the type of material and its composition as well as its electrical and physical properties are very important and directly affect cell performance [51].

The objective of this chapter is to describe the simulation software SILVACO-ATLAS and its implementation in the framework for Investigation of the electrical characteristics and the photo-parameters of the InGaN-based solar cell by considering its related structure configurations.

III.2 Modeling today

There is a very large number of publications available that document the modeling of almost every aspect of solar cell function and behavior. These span from the macroscopic electrical to the microscopic molecular level and have very high accuracy and credibility. However, they all address individual solar cell viewpoints, without providing complete coverage of the complex combination of phenomena that actually take place. Thus, there is a need to select and use a large number of different models, in order to study an actual complete cell structure. An important consideration is a fact that not all of these models are compatible with each other. This makes their selection prone to errors, quite hard, and time consuming. In addition, each one exposes the researcher to many detailed parameters that usually create a lot of unnecessary confusion. All the above make a complete simulation of advanced solar cells a hard task [52].

As a consequence, solar cell research today is conducted by actually fabricating cells and experimenting with them. Then, researchers theorize about the collected results. Although that

methodology provides the most credible results, it may also lead to some confusion. The reason lies in the huge number of factors that always need to be considered, most of which are more relevant to the fabrication process used and not the cell itself. Therefore, many combinations of parameters need to be materialized like material types and characteristics, doping, dimensions, fabrication conditions, and processes. This is not only time and personnel consuming task, but can also be expensive to carry out. The number of experiments, needed to answer questions, is also very large because experts are not allowed to focus on a certain issue. Instead, they need to consider and develop the design and the complete fabrication process of the cell under study. Additionally, in any kind of experiment, there is always a number of unpredictable factors that may introduce deviation among results [52].

III .3 SILVACO

SILVACO (Silicon Valley Corporation) is an American international company that specializes in the creation of simulation software headquartered in Santa Clara, California. This company is one of the leading suppliers of channels finite element simulation software and design-assisted computer for electronics technology TCAD (Technology Computer Aided Design) targeting almost every aspect of modern electronic design[53].

The company provides modeling and simulation capabilities for simple Spice–type circuits all the way to detailed VLSI circuits (Very Large Scale Integration) fabrication (Figure III.1). User–friendly environments are used to facilitate the design and a vast number of different modeling options. The tools provide for creating complex models and 3D structural views[52].
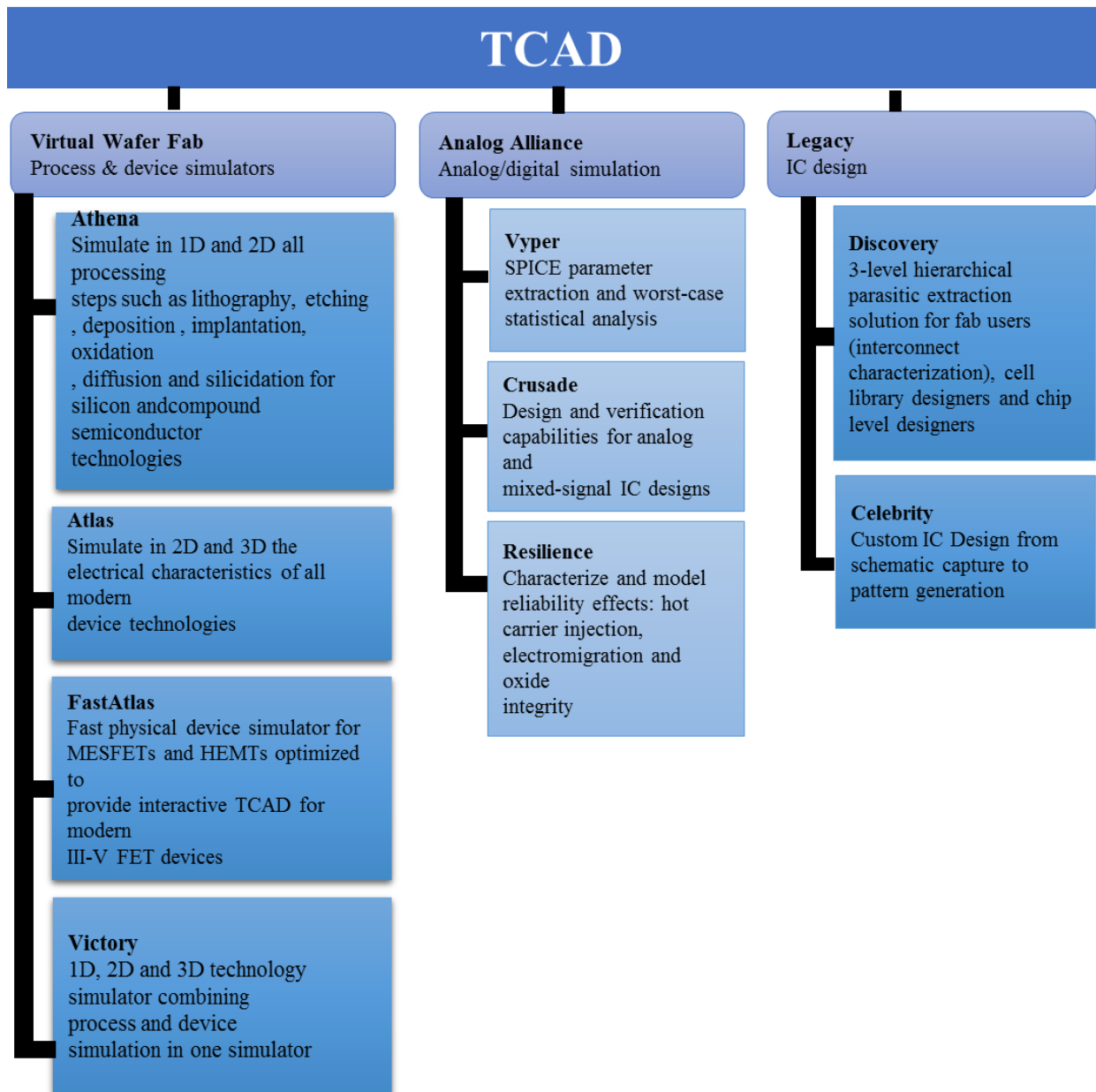
Figure III. 1: Silvaco's T CAD suite of tools [54].

❖ SILVACO presents a set of interactive simulation tools for the design and analysis of most VWF (Virtual Wafer Fabrication) semiconductor devices (Figure III-2). The basic components of VWF are:

III.3.1 The simulation tools (VWF CORE TOOLS)

These tools simulate either their manufacturing process or their electrical behavior. The simulation tools are ATHENA, ATLAS, and SDUPEM3.

❖ **ATLAS:** Physical simulator of 2D or 3D semiconductor devices that simulates the electrical behavior of specified structures of semiconductor devices [53].

❖ **ATHENA:** a 2D simulator of technological processes that allows developing and optimizing semiconductor manufacturing processes (the different steps performed in the White Room). It provides a platform for simulating ion implantation, diffusion, etching, deposition, lithography, oxidation, and solicitation of semiconductor materials. It replaces expensive experiments with simulations [53].

❖ **SSUPEMS3:** 1D process simulator with simple extensions of device simulations[53].
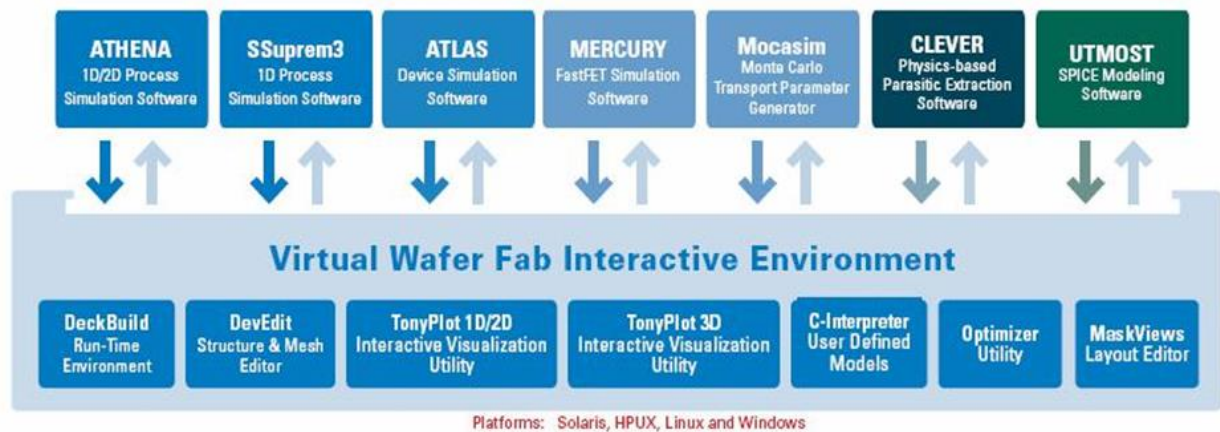
Figure III. 2: The environment of the VWF[55].

III.3.2 Interactive tools (VWF INTERACTIVE TOOLS)

These tools are designed to be used in the interactive mode in constructing a single input file. Being based on a user interface that is graphical (GUI). Thus, the work of construction of the input file becomes more efficient. Interactive tools can be used either in conjunction with a set of files or as components built into the automation tools environment.

III.3.3 Automation tools (VWF AUTOMATION TOOLS)

These tools allow the user to perform large-scale experimental studies to create results for the following static analysis. Automatic tools use distributed database technology and interprocess development software methods.

III.4 Working with Atlas

Atlas can accept structure description files from Athena and Devedit, but also from its own command files, the development of the desired structure in Atlas is done using a declarative programming language. This is interpreted by the Atlas simulation engine to produce results [56].

The first line to be read by the program when running ATLAS using DeckBuild is the GO ATLAS command. After that, the structure of the statement should be followed in the sequence depicted in figure III.3 if the order is not respected, an error message appears and the program does not execute correctly. An ATLAS statement is comprised of a keyword and a set of parameters, which are not case sensitive, in the following format [57]:
<STATEMENT> <PARAMETER>=<VALUE>.
A brief walk–through of how a structure is built and simulated follows.

Figure III. 3: Command group and statements layout for a Silvaco **ATLAS** file [57].

III.4.1 Mesh

The grid consists of horizontal and vertical lines with a user-defined distance between them. It bounds the physical area of the cell by creating a number of triangles in which the simulation will take place [56].

The first thing that needs to be specified is the mesh on which the device will be constructed this can be 2D or 3D and can be comprised of many different sections. Orthogonal and cylindrical coordinate systems are available. Several constant or variable densities can be specified while scaling and automatic mesh relaxation can also be used. This way, a number of minimum triangles are created; this determines the resolution of the simulation. The correct specification of the mesh is very important for the final accuracy of the results. If the number or density of triangles is not high, enough in regions, such as junctions or material boundaries, the results of the simulation will be crude and possibly misleading. On the other hand, the use of too many triangles will likely lead to significant and unnecessary increases in execution time, So a fine defined mesh will lead to more accurate results, and on the other hand, a coarse mesh that minimizes the total number of grid points will lead to a larger numerical efficiency[52, 56]. An example of both fine and coarse meshes designed in ATLASTM is depicted in Figure III.4
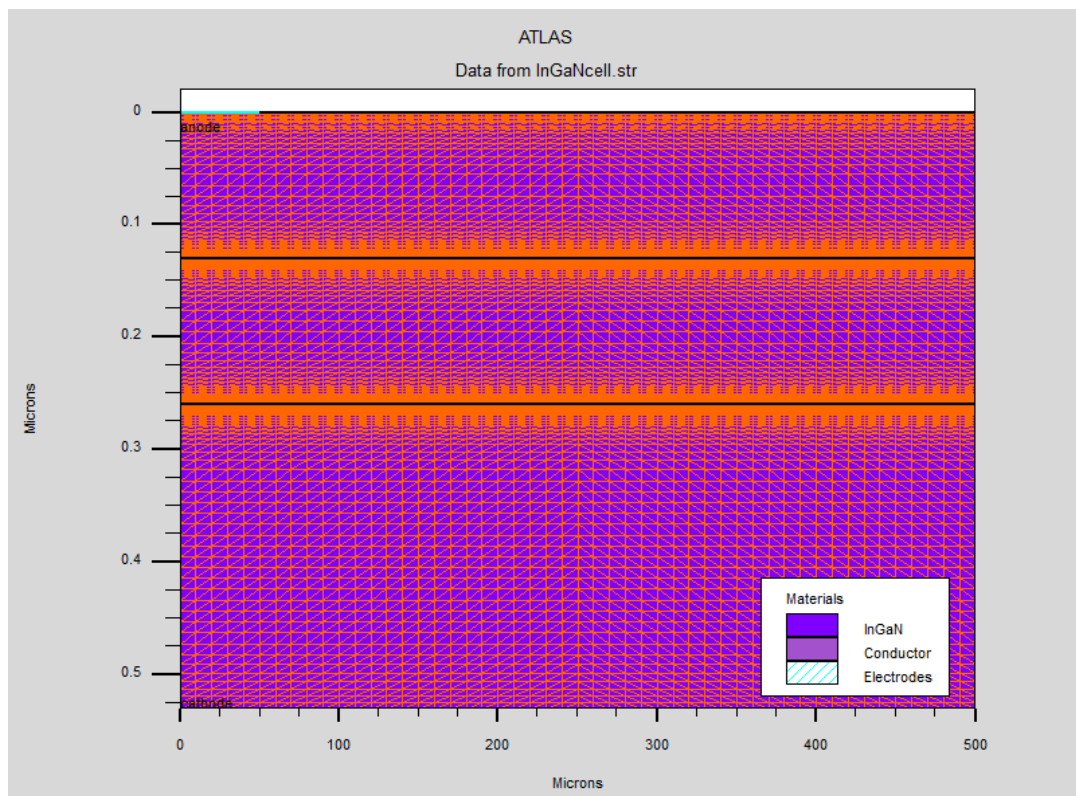
Figure III. 4: Typical mesh in ATLAS.

III.4.2 Region

The next step in creating a semiconductor device is to separate the created mesh into regions. The format to define the regions is:

REGION number=<integer> <material type>

<Position parameters>.

This statement can be broken up into several parts. First, the selected integer creates a region that can be referred to by that same integer. The material type determines what element or compound this region becomes and must be available in the ATLAS database. This can be selected out of Silvaco's own library or can be custom–made by the user. In addition, heterojunction grading between materials can also be described. Last, the position parameters tell ATLAS which potion of the mesh that was just created will become the region [57].

An example of created regions can be found in Figure III.5.
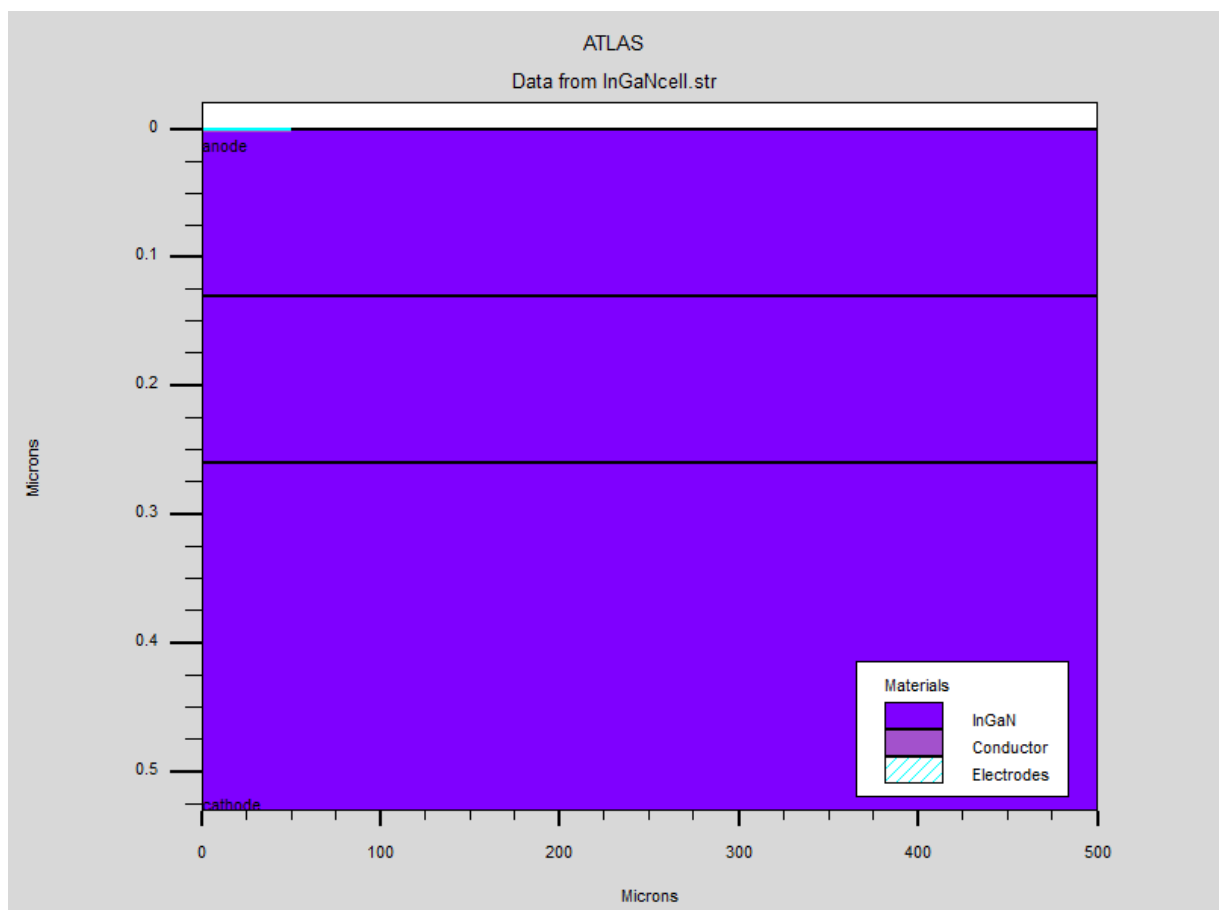
Figure III. 5: Specified Regions.

III.4.3 Contacts

After defining the regions and materials, the next step is to create contacts on the device. To define the electrodes of the device, their position and size need to be entered. Additional information about their materials and work functions can be supplied if needed [52]. The format to define the electrodes is:

ELECTRODE NAME = <electrode name> <position>.

BOTTOM and TOP statements specify that the electrode be positioned along the bottom or the top of the device, respectively. Otherwise, minimum and maximum position boundaries must be specified, using the X.MIN, X.MAX, Y.MIN, Y.MAX statements [56].

An observation, in this work the only electrodes defined, are the anode and the cathode. However, Silvaco Atlas has a limit of 50 electrodes that can be defined [55].

III.4.4 Doping

After creating the separate regions and assigning materials to those regions, the materials themselves can be doped. The user specifies the doping using the DOPING statement:

DOPING <distribution type> <dopant type> <position parameters>.

The DOPING statement is broken down into three sections.

First, the distribution type can be either uniform, Gaussian, or complementary error function forms, only the uniform distribution type is utilized in this work. Next, a concentration and type of doping must be specified. Finally, the region to be doped must be identified [58].

III.4.5 Material

The previously defined and doped region must be associated with specific materials. Materials used throughout the simulation can be selected from a library that includes a number of common elements, compounds, and alloys. These have their most important parameters already defined. However, in solar cells, the use of exotic materials is not unusual. For such purposes, there is the ability to fully define already existing or brand new materials, down to their smallest detail. Such properties range from the essential bandgap and mobility all the way to light absorption coefficients. Contact information and work functions can also be entered here [52].

The general MATERIAL statement is:

MATERIAL <localization> <material definition>.

III.4.6 Models

More than seventy models can be used to achieve a better description of a full range of phenomena. Each model can be accompanied by a full set of its parameters when these differ from the default. Again, new models can be described using the C interpreter capability [52]. The physical models are grouped into five classes: mobility, recombination, carrier statistics, impact ionization, and tunneling. The list of physical models available to the ATLAS software can be found in the ATLAS user's manual [57]. The general MODELS statement is:

MODELS <model name>.

A specific example that specifies standard concentration dependent mobility, parallel field mobility, Shockley-Read-Hall recombination with fixed carrier lifetimes, and Fermi Dirac statistics is:

MODELS CONMOB FLDMOB SRH FERMIDIRAC.

III.4.7 Light Beam

When lighting is important for a device (like in solar cells), there is the ability to use a number of light sources and adjust their location, orientation, and intensity. The spectrum of the light can be described in all the necessary detail. Polarization, reflectivity, and ray trace are also among the simulator's features [52]. An optical beam is modeled as a collimated source using the BEAM statement of the form:

BEAM <parameters>.

The origin of the beam is defined by parameters X. ORIGIN and Y. ORIGIN, the ANGLE parameter specifies the direction of propagation of the beam relative to the x-axis, while ANGLE=90 describes a vertical illumination from the top of the device.

The beam is automatically split into a series of rays so that the sum of the rays covers the entire width of the illumination window. When the beam is split, ATLAS automatically resolves discontinuities along the region boundaries of the device. Rays are also split at interfaces between regions into a transmitted ray and a reflected ray [56].

For the purposes of this work, the source is the sun, and the AM1.5 spectrum is used to simulate the energy received by a solar cell in a terrestrial application.

III.4.8 Solution Method

ATLAS contains several numerical methods to calculate the solutions to semiconductor device problems. There are three main types of numerical methods. The first method is the GUMMEL type, which is useful where the system of equations is weakly coupled but has only linear convergence. The next method is NEWTON, which is useful when the system of equations is strongly coupled and has quadratic convergence. This method causes ATLAS to spend extra time solving for quantities, which are essentially constant or weakly coupled and requires a more accurate initial guess to the problem to obtain convergence. The final method is the BLOCK method, which can provide faster simulation times in situations where the NEWTON method struggles. Numerical methods are given in the METHOD statements of the input file [58]. An example of an efficient METHOD statement is:

METHOD GUMMEL BLOCK NEWTON.

III.4.9 Solution Specification

This section of the input deck to ATLAS is where the simulation does its calculations to solve for the device specified. It is divided up into four parts: LOG, SOLVE, And LOAD

↓ The LOG

the statement creates a save file where all results of a run will be saved; Any DC, transient or AC data generated by "SOLVE" statements after the "LOG" statement will be saved [59]. An example LOG statement in which data is saved into example.log is:

LOG OUTFILE = example.log.

↓ The SOLVE

Solve statement follow the log statement and instructs Atlas to perform a solution for one or more specified bias points after getting an initial guess by solving the only Poisson equation,

which means a simplified initial solution [50]. An example SOLVE statement that ramps the anode voltage from 0.0 V to 3.0 V with 0.01 V steps w is:

SOLVE VANODE=0.0 VSTEP=0.01 VFINAL=3.0 NAME=ANODE.

The LOAD and SAVE

Statements are used together to help create better initial guesses for bias points. The SAVE statement is used first to store all of the information about the bias points, and later the LOAD statement is used to retrieve that information and aid in the solution [58]. The following are examples of the LOAD and SAVE instructions.

SAVE OUTF = SOL.STR

LOAD INFILE = SOL.STR.

III.4.10 Data Extraction and Plotting

The final section of the input deck is extracting the data and plotting it in a useful way. The two statements associated with this section are EXTRACT and TONYPLOT [58].

Extract

The EXTRACT command allows extracting device parameters. It operates on the previous solved curve or structure file. By default, EXTRACT uses the currently open log file. To override this default, supply the name of a file to be used by EXTRACT before the extraction routine [60]. The EXTRACT statement is:

EXTRACT INIT INF="<filename>".

TonyPlot

All graphics in Atlas is performed by saving a file and loading the file into TonyPlot. The TONYPLOT command causes Atlas to automatically save a structure file and plot it in TonyPlot. The TonyPlot window will appear displaying the material boundaries. Plot: Display menu is used to see more graphics options [57]. The TONYPLOT statement is:

TONYPLOT "<filename>".

Chapter IV:

Qualitative study of Indium Gallium Nitride ($InGaN$) – based solar cell.

IV.1 Introduction

While $GaN/InGaN$ heterojunction and $InGaN$ homojunction solar cells have been demonstrated using Ga-rich materials, their efficiencies and performances are still poor, mainly due to theoretical limits or transparency loss for high-bandgap-energy $InGaN$ cells because of low in composition and poor crystalline quality of the grown $InGaN$ cells. Although various efforts have been carried out toward the goal of high-efficiency solar cells from different viewpoints, however, still there are many challenges to achieve such a goal.

In this chapter, we will study three PIN structures based on $InGaN$ from a simple structure configuration of the solar cell reflecting the ideal case to a more realist structure closer to the experimental cell. This study will take into account a wide range of energy (by changing the molar fraction of indium x_{In}). The three structures will be investigated under light condition of the standard global solar spectrum AM1.5 .We will also study the defects effect, the $P - GaN$ and $I - InGaN$ layers effect on the third structure. The study is mainly by numerical simulation using, as a tool, the SILVACO-ATLAS software. This latter allows us to calculate the device performance parameters such as the current density-voltage and the power-voltage characteristics, (J-V) and (P-V) respectively, the short-circuit current density (Jsc), the open-circuit voltage (Voc); the maximum power ($Pmax$) delivered by the cell, the fill factor (FF), and the conversion efficiency (η).

IV.2 Simulation Parameters

IV.2.1 Structures Specifications

In our work, we have selected three structures (A, B and C) to study for the PIN $In_xGa_{1-x}N$ based solar cell, with a total surface of 1 cm^2 and exposed to the solar radiation AM1.5.

↯ Structure A

$In_xGa_{1-x}N$ based solar cell with a single homojunction PIN structure (See Figure IV .1) which consists of three layers: $P - In_xGa_{1-x}N$ layer with a thickness of $0.13\mu m$ and doping $N_a = 5 \times 10^{17} cm^{-3}$; $I - In_xGa_{1-x}N$ layer with a thickness of $0.13\mu m$ and $N - In_xGa_{1-x}N$

layer doped with $N_d = 5 \times 10^{17} cm^{-3}$ and thickness of $0.27 \mu m$; the anode covers only $50 \mu m$ of the total width of the cell (500μm) so that the majority of the upper cell surface is exposed to light. The cathode, on the other hand, extends over the entire width of the cell.
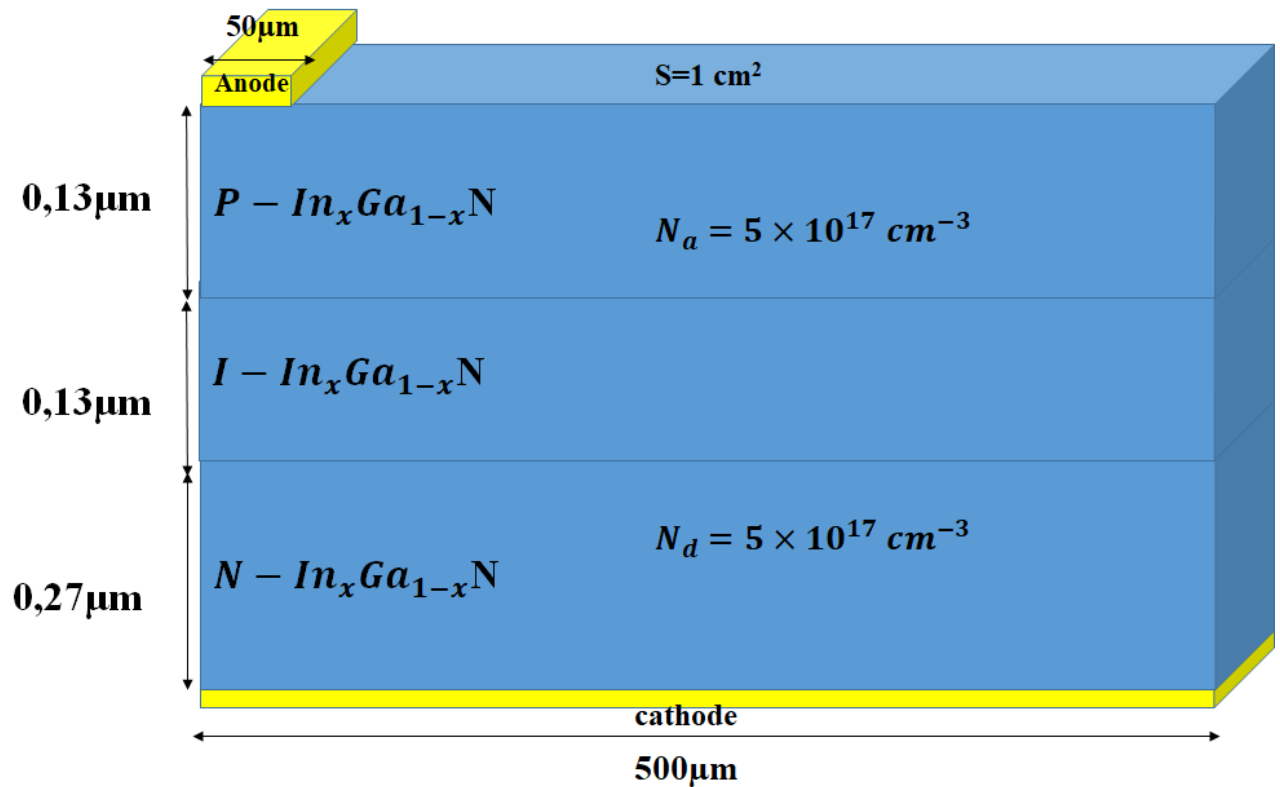
Figure IV. 1: *InGaN* based solar cell with homojunction PIN structure.

✚ Structure B

$P - GaN/I - In_xGa_{1-x}N/N - In_xGa_{1-x}N$ heterojunction P-I-N solar cell (as show in Figure IV.2). The first $P - GaN$ layer has a thickness of $0.13 \mu m$ and doped with $N_a = 5 \times 10^{17} cm^{-3}$, the second I-$In_xGa_{1-x}N$ layer has a thickness of $0.13 \mu m$ and the third N-$In_xGa_{1-x}N$ layer has a thickness of $0.27 \mu m$ and doped with $N_d = 5 \times 10^{17} cm^{-3}$.
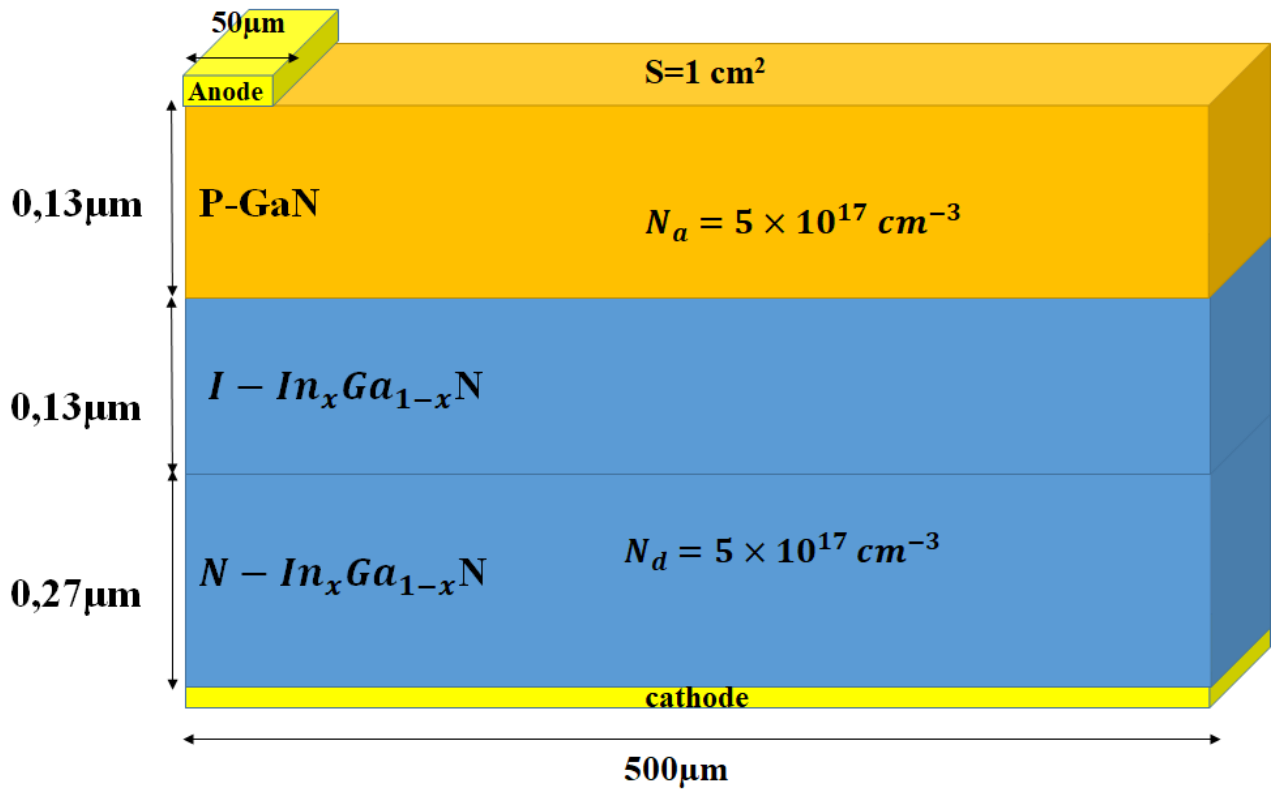
Figure IV. 2: GaN/InGaN heterojunction solar cell with PIN structure.

⬇ Structure C

$P - GaN/I - In_xGa_{1-x}N/N - GaN$ double heterojunction solar cell with PIN structure placed on sapphire substrate (see Figure IV.3). The $p - GaN$ layer has thickness of $0.13\mu m$ and doping $N_a = 5 \times 10^{17} cm^{-3}$, the I-$In_xGa_{1-x}N$ layer thickness is $0.13\mu m$ thick, the $N - GaN$ with thickness of $0.27\ \mu m$ and doping $N_a = 5 \times 10^{17} cm^{-3}$; the GaN buffer layer with thickness of $2\ \mu m$ and sapphire substrate with $20\mu m$ of thickness. The anode covers only $50\mu m$ of the total width of the top of the cell so that the majority of the upper cell surface is exposed to light, the cathode is placed beside them $N - GaN$ layer.

Qualitative study of Indium Gallium Nitride (InGaN) – based solar cell.
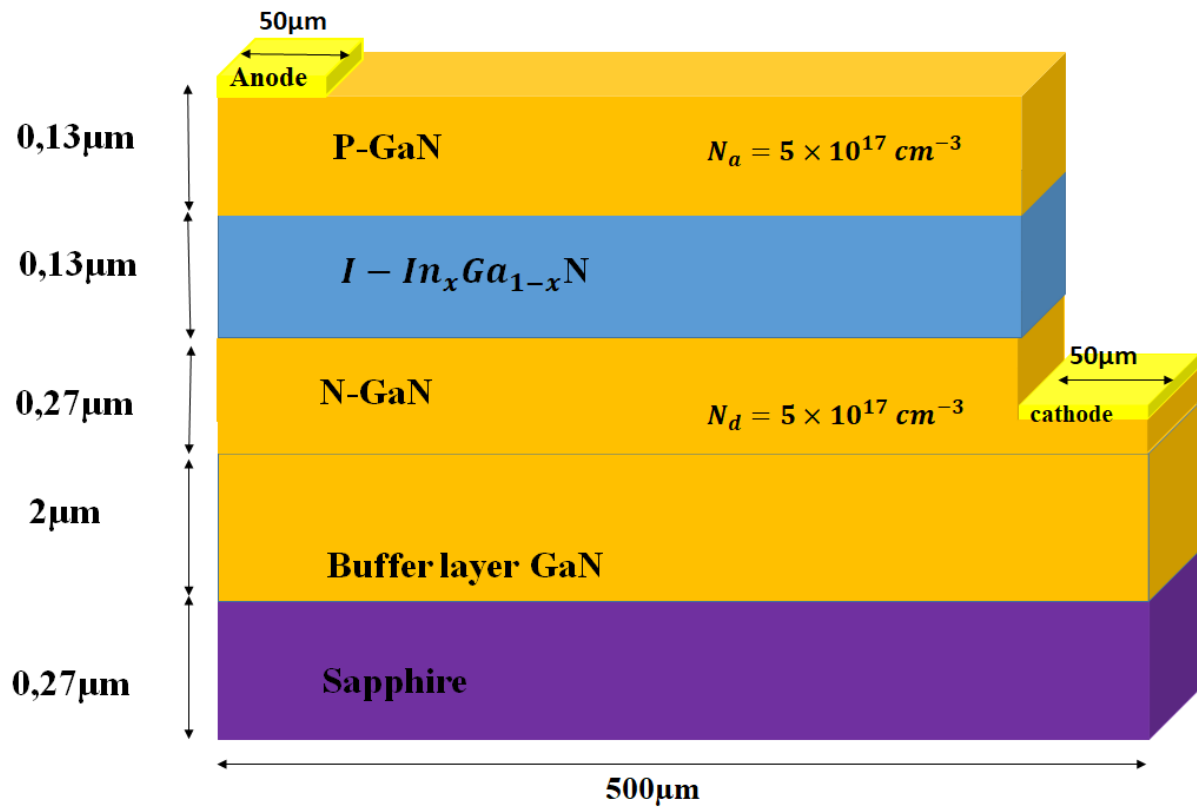
Figure IV. 3: GaN/InGaN double heterojunction solar cell with PIN structure.

The SILVACO-ATLAS presentation of the studied structures of the cell; is illustrated in the figures (IV.4), (IV.5), (IV.6), (IV.7), (IV.8) and (IV.9) respectively.

Qualitative study of Indium Gallium Nitride (InGaN) – based solar cell.
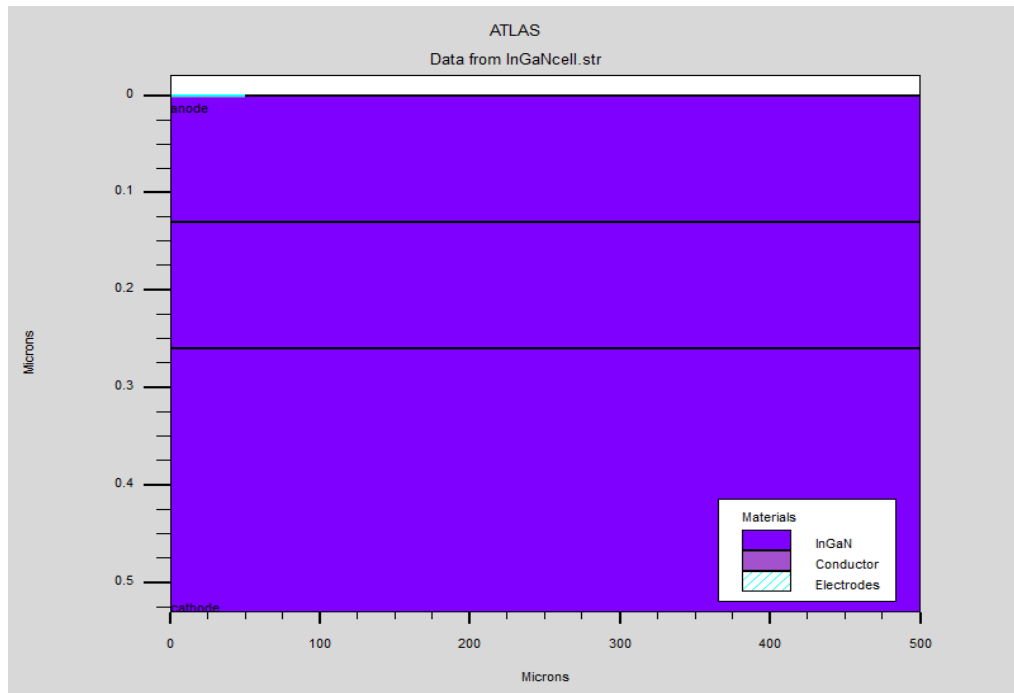
Figure IV. 4: Structure of InGaN-based homojunction solar cell (structure A) under the Silvaco-Atlas simulator.
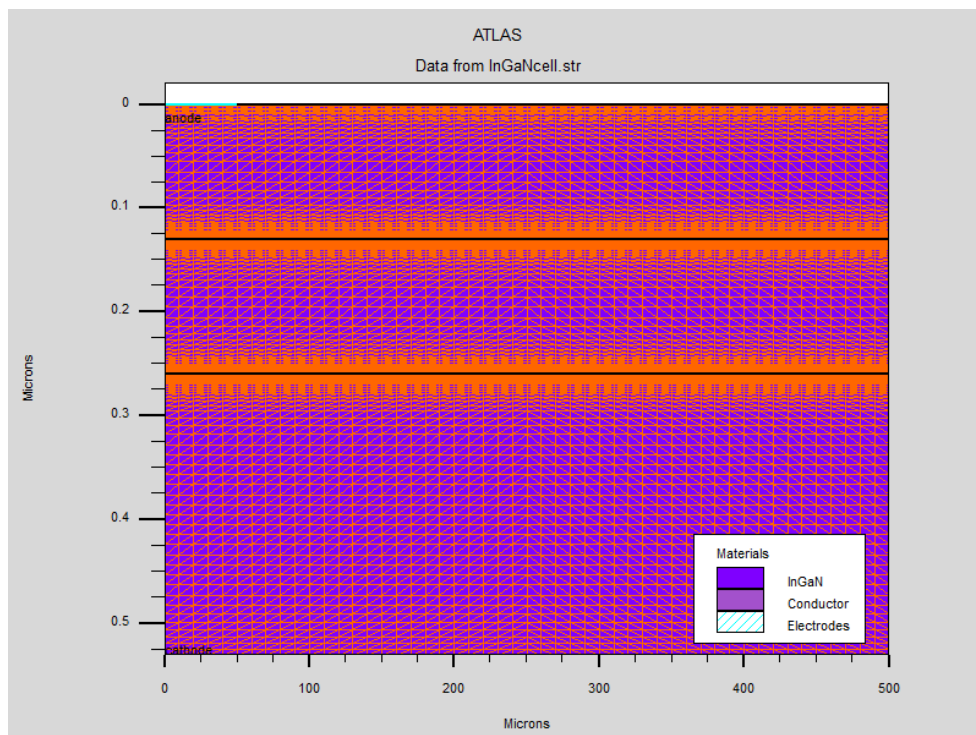
Figure IV. 5: Spatial mesh of the homojunction solar cell (structure A) under the Silvaco-Atlas simulator.

Qualitative study of Indium Gallium Nitride (InGaN) – based solar cell.
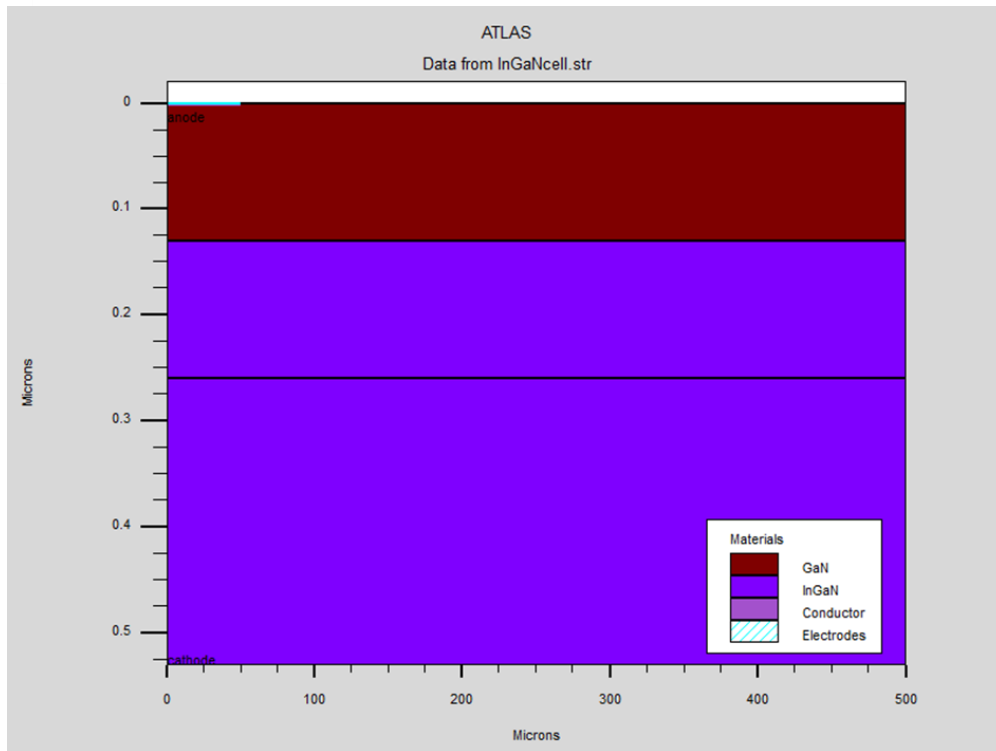
Figure IV. 6: Structure of GaN/InGaN heterojunction solar cell (structure B) under the Silvaco-Atlas simulator.
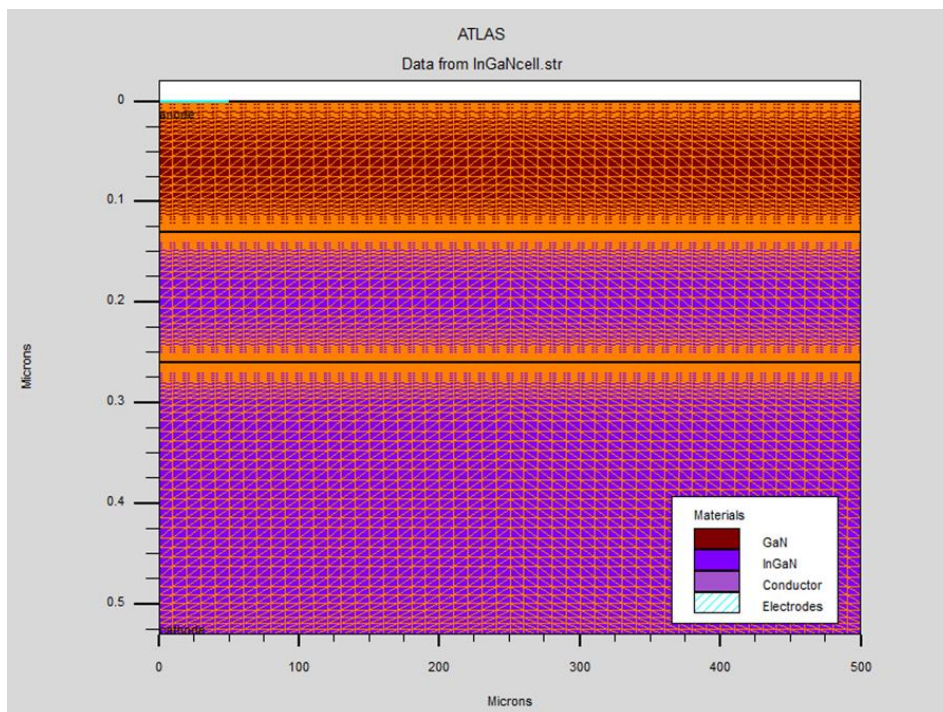
Figure IV. 7: Spatial mesh of the heterojunction solar cell (structure B) under the Silvaco-Atlas simulator.
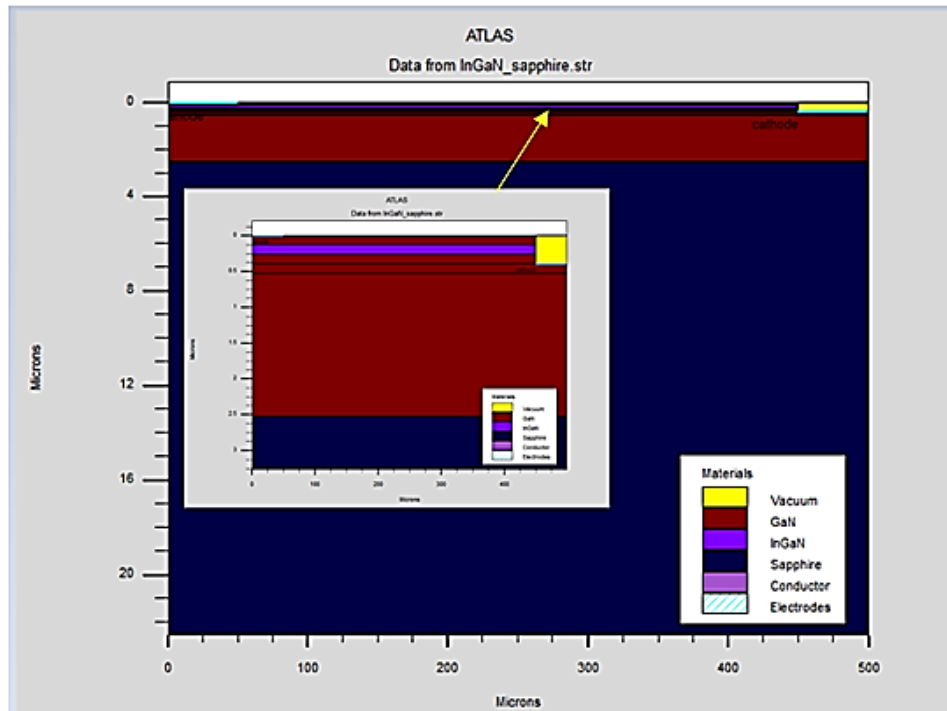
Figure IV. 8: Structure of the GaN/InGaN double heterojunction solar cell (structure C) under the Silvaco-Atlas simulator.
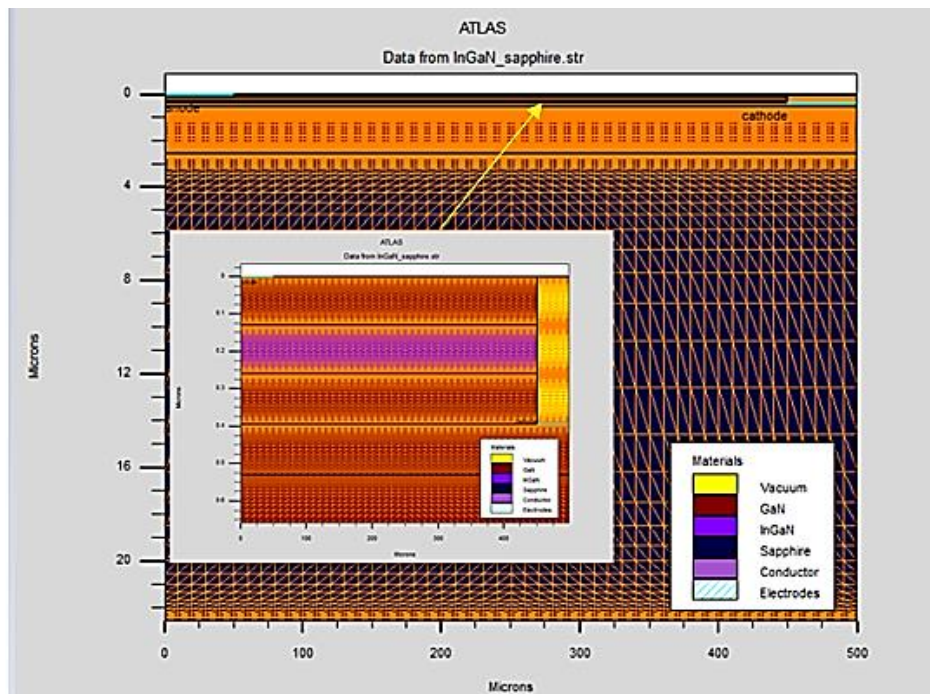
Figure IV. 9: Spatial mesh of the double heterojunction solar cell (structure C) under the Silvaco-Atlas simulator.

IV.2.2 Input Parameter values

The simulation parameters associated with the studied solar cells are shown in Table IV.1 taking into account the Silvaco database.

Table IV. 1: Simulation parameters associated with the cells studied taking into account the database of Silvaco data.

Material	$InGaN$	GaN	Al_2O_3
Type	Semi-conductor		Insulator
The Goal	Basic material	Optical Windows collector	
Permittivity ε_r	$15.3x + 8.9(1-x)$ [43].	8.9	12
Affinity (ev)	$3.659x - 2.666x^2 + 4.31$ [61]		
Band gap E_g (eV)	E_g (x_{In}) =3.42x+0.77(1-x)-1.43x (1-x) [36].	3.42	
The effective density of states for electrons $N_C(cm^{-3})$	$0.9 + 2.3(1-x).10^{18}$ [62].	2.24×10^{18}	
The effective density of states for holes $N_v(cm^{-3})$	$5.3x + 1.8(1-x).10^{19}$ [62].	2.51×10^{19}	
Doping(cm^{-3})	5×10^{17}	5×10^{17}	
The Lifetime(sec) $\tau_n = \tau_p$	1×10^{-9} [42].	6.5×10^{-9}[63].	
Mobility electron $(cm^2 V^{-1} S^{-1})$	$524x + \mu_n(GaN)$[61].	1000[64].	
Mobility hole $(cm^{-1} V^{-1} S^{-1})$	$6.5x + \mu_p(GaN)$[61].	350[64].	

Optical parameters (extinction coefficient k in terms of wavelength λ for different concentrations of indium x_{In}) (see Figure IV.10).

We calculated the extinction coefficient k from the absorption coefficient according to the following theoretical model $\alpha(\lambda)$:

$$\alpha(\lambda) = a_0 \sqrt{a(x)(E - E_g) + b(x)(E - E_g)^2}$$

With: $E = \dfrac{hc}{\lambda}$ **(IV.1)**

The dimensionless fitting parameters $a(x)$ and $b(x)$ are given for small indium content [40]. For more details and to consider all the indium content compositions, we use further adjustment parameters a_{fit} and b_{fit} [40]. A linear interpolation is used to find the new fitting parameters over the entire composition range. In this case, the wavelength-dependent absorption coefficient has been determined for all alloy compositions. The parameters a_{fit} and b_{fit} are given using this linear interpolation [41]:

$$a_{fit} = 12.87x^4 - 37.79x^3 + 40.43x^2 - 18.35x + 3.52 \qquad \textbf{(IV.2)}$$

$$b_{fit} = -2.92x^2 + 4.05x - 0.66 \qquad \textbf{(IV.3)}$$

The extinction coefficient k is related to the absorption coefficient α following the equation:

$$\alpha = \dfrac{4\pi}{\lambda} k \qquad \textbf{(IV.4)}$$

Then, we can calculate the extinction coefficient k required to be added as data file in Silvaco-Atlas:

$$k = \dfrac{\alpha\lambda}{4\pi} \qquad \textbf{(IV.5)}$$

In our simulations, we will use the Adachi model, which is used to calculate the refractive index of the materials and the equation that represents this model is [43]:

$$n_r(\omega) = \sqrt{A\left(\dfrac{\hbar\omega}{E_g}\right)^{-2}\left\{2 - \sqrt{1 + \dfrac{\hbar\omega}{E_g}} - \sqrt{1 - \dfrac{\hbar\omega}{E_g}}\right\} + B} \qquad \textbf{(IV.6)}$$

Where E_g is the bandgap, ω is the optical frequency and A and B are material composition dependent parameters. For $In_xGa_{1-x}N$, the compositional dependence of the A and B parameters are given by the expressions in Equations II.7 and II.8 respectively[43].

$$A(x) = 9.827(1 + x) - 53.57x \tag{IV.7}$$

$$B(x) = 2.736(1 - x) - 9.19x \tag{IV.8}$$
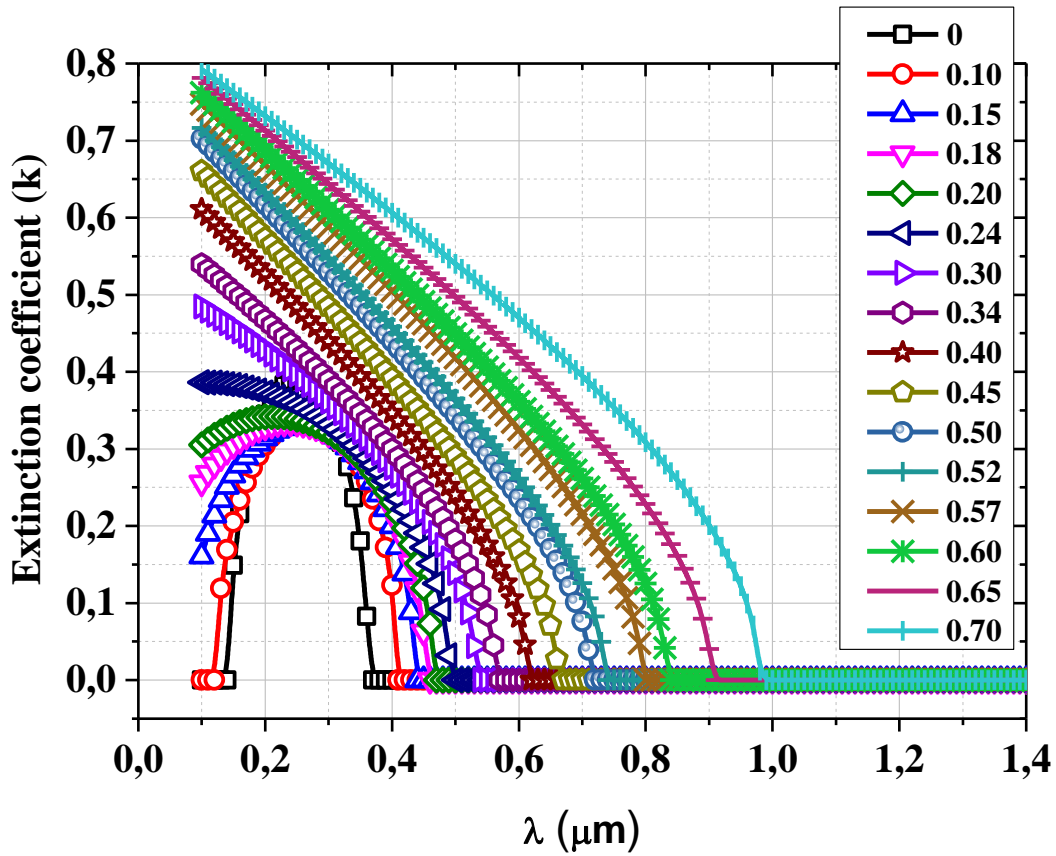
Figure IV. 10: Extinction coefficient k in terms of wavelength λ for different concentrations of indium x_{In} according to theoretical calculations[40, 41].

IV.3 Results and discussions

Figure IV.11 shows the energy gap profile of the three studied cells at thermal equilibrium. The alignment between the two quasi Fermi levels, E_{fn} for the electrons and E_{fp} for holes, is well verified at thermal equilibrium for the three cells. In structures B and C, the discontinuity in E_C or E_V, at GaN/InGaN interfaces, can form a considerable barrier against electron and hole transport within the i-layer when the InGaN band gap width is reduced enough, and this case deteriorates considerably the cell performances. For this reason, the InGaN band gap should be tuned carefully taking into account the discontinuity value in E_C or E_V at GaN/InGaN interfaces. As the InGaN band gap becomes wider, the discontinuity effect is reduced remarkably.
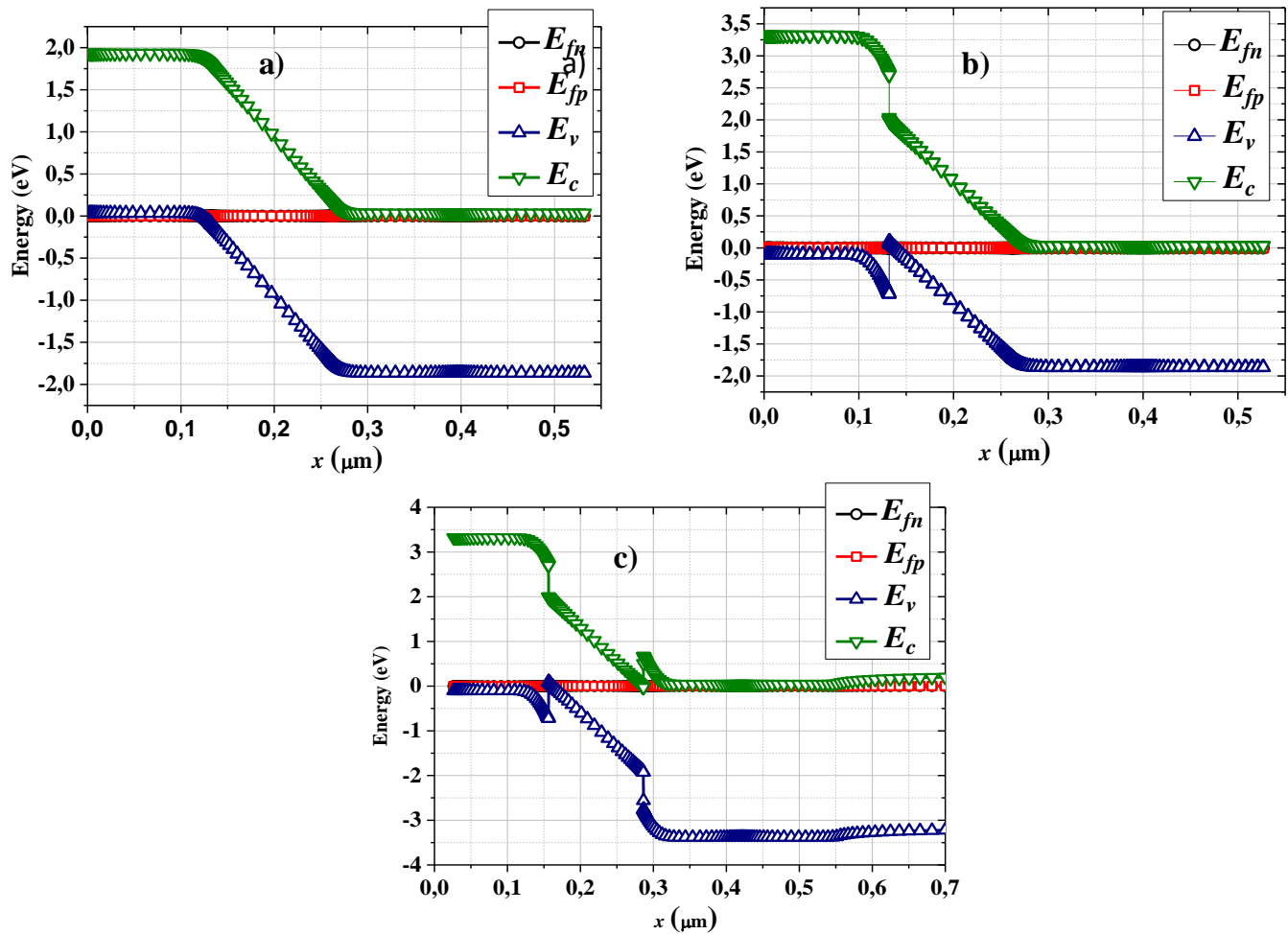
Figure IV. 11: Energy gap profile of the three studied cells at thermal equilibrium: (a) structure A, (b) structure B and (c) structure C.

Figures IV.12 present, respectively, the current density - voltage $(J - V)$ and the power - voltage (P-V) electrical characteristics corresponding to the three studied cells A, B and C with in molar fractions of x_{In}=0.24 , $x_{In} = 0.34$ and $x_{In} = 0.57$.

Qualitative study of Indium Gallium Nitride (InGaN) – based solar cell.
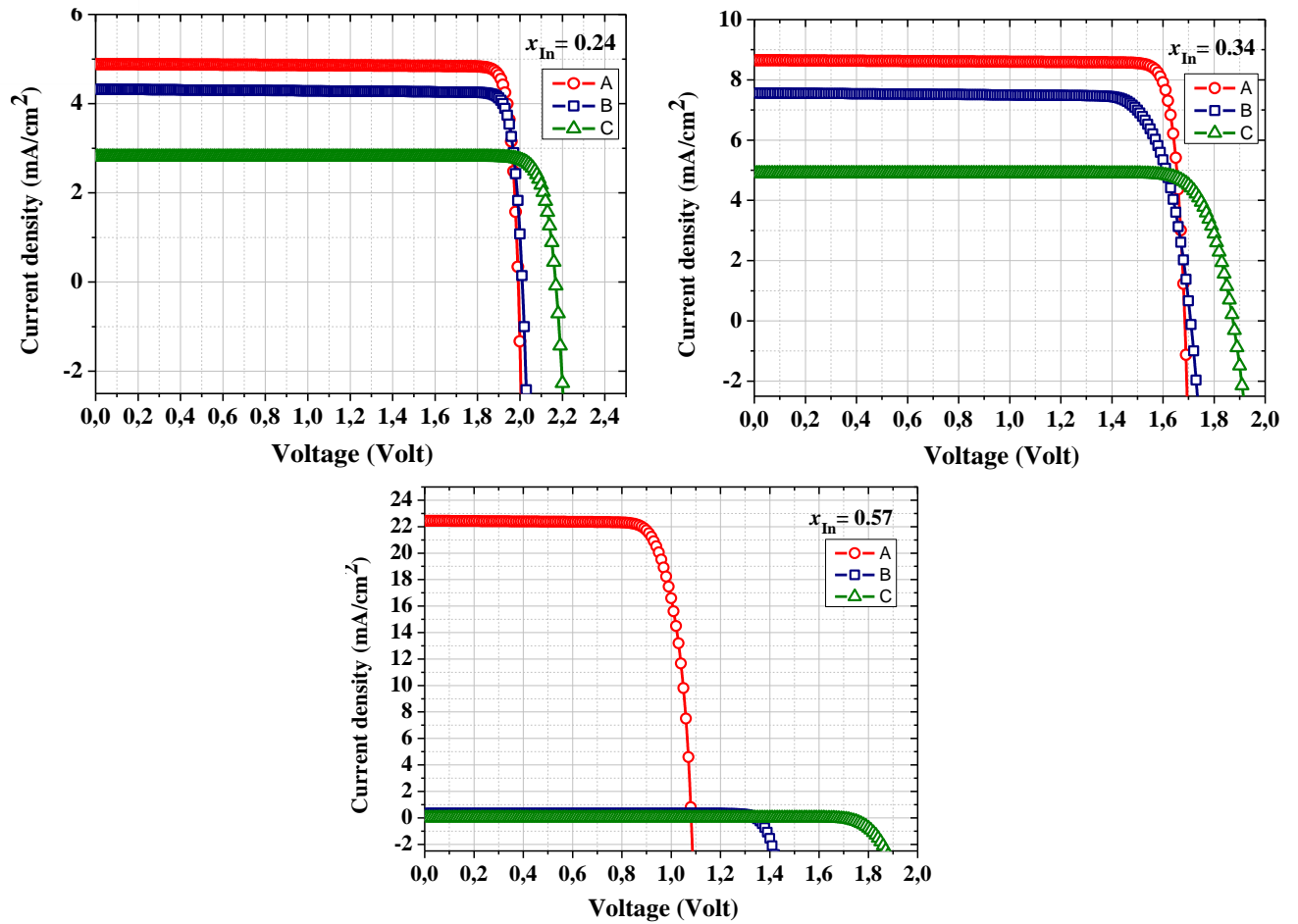
Figure IV. 12: Current density - voltage $(J - V)$ electrical characteristics of the studied solar cells A, B and C with x_{In}=0.24 , $x_{In} = 0.34$ and $x_{In} = 0.57$, under AM1.5 illumination.
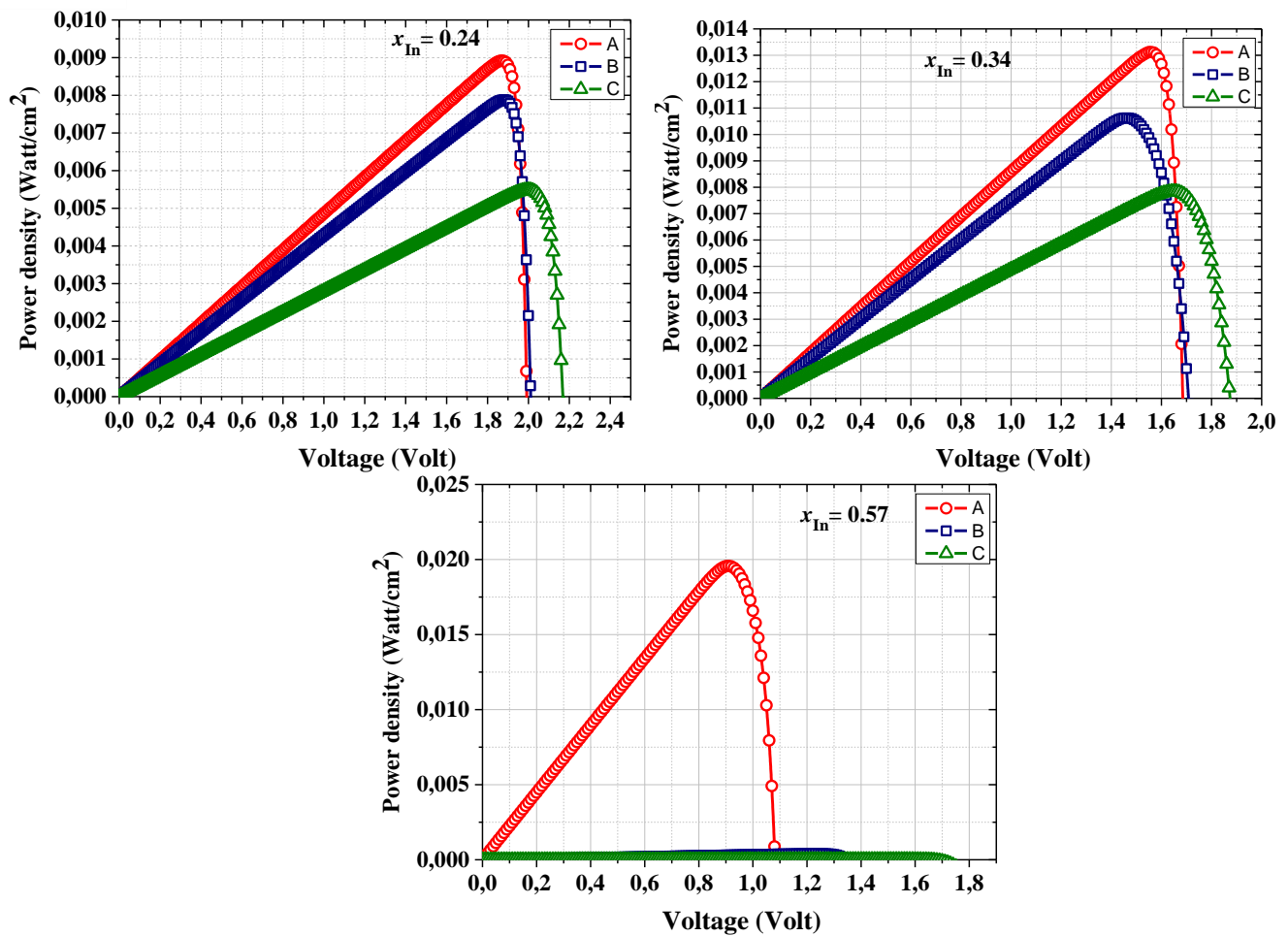
Figure IV. 13: Power - voltage $(P - V)$ characteristics of the studied solar cells A, B and C with x_{In}=0.24 , $x_{In} = 0.34$ and $x_{In} = 0.57$, under AM1.5 illumination.

Table IV.2 presents all results of the cell output parameters (the short-circuit current density (Jsc), the open-circuit voltage (Voc), the fill factor (FF), and the conversion efficiency (η)) obtained by changing x_{In} for each cell structure: A, B and C. In addition, figures IV.14 plots the cell output parameters variation for the structures A, B and C when indium molar fraction x_{In} is changed.

Chapter IV

Qualitative study of Indium Gallium Nitride (InGaN) – based solar cell.

Table IV. 2: Cell output parameters variation for the structures A, B and C with changing the indium molar fraction x_{In}

Cellule	x_{In}	J_{sc} (mA/cm²)	V_{oc} (Volt)	FF (%)	P_m (Watt/cm²)	η (%)
A	0.10	1.41627	2.45824	93.0326	0.00323896	3.23896
	0.15	2.38118	2.28733	92.6103	0.00504406	5.04406
	0.18	3.12931	2.18711	92.3060	0.00631756	6.31756
	0.20	3.63954	2.12116	92.1060	0.00711063	7.11063
	0.24	4.88716	1.99203	91.6343	0.00892094	8.92094
	0.30	7.00157	1.80485	90.7699	0.01147040	11.4704
	0.34	8.65157	1.68522	90.0198	0.01312470	13.1247
	0.40	11.5430	1.51376	88.5366	0.01547030	15.4703
	0.45	14.3996	1.37859	86.8106	0.01723290	17.2329
	0.50	17.6315	1.25021	84.5871	0.01864560	18.6456
	0.52	18.9294	1.20063	83.6029	0.01900060	19.0006
	0.57	22.4466	1.08162	80.6048	0.01956980	19.5698
	0.60	24.6807	1.01358	78.4650	0.01962870	19.6287
	0.65	28.5985	0.906162	74.3280	0.01926200	19.262
	0.70	31.6987	0.805268	70.0589	0.01788320	17.8832
B	0.10	1.31183	2.47546	92.5552	0.003005620	3.00562
	0.15	2.1619	2.30504	91.9548	0.004582350	4.58235
	0.18	2.80484	2.20516	91.5508	0.005662530	5.66253
	0.20	3.25072	2.13967	91.283	0.006349160	6.34916
	0.24	4.3206	2.01126	90.6971	0.007881440	7.88144
	0.30	6.14569	1.82559	89.4905	0.010040400	10.0404
	0.34	7.56235	1.70845	82.2832	0.010630900	10.6309
	0.40	1.80642	1.56214	32.3767	0.000913632	0.913632
	0.45	0.440902	1.48604	73.7127	0.000482964	0.482964
	0.50	0.353691	1.42396	87.3960	0.000440163	0.440163
	0.52	0.349395	1.40056	88.1762	0.000431489	0.431489
	0.57	0.347395	1.34341	88.3817	0.000412472	0.412472
	0.60	0.347435	1.31103	88.2562	0.000402005	0.402005
	0.65	0.347746	1.25936	87.9975	0.000385374	0.385374
C	0.10	0.950938	2.61847	91.4336	0.002276700	2.2767
	0.15	1.480410	2.45369	91.1474	0.003310900	3.3109
	0.18	1.869640	2.3568	90.8637	0.004003790	4.00379
	0.20	2.149100	2.29302	90.6573	0.004467530	4.46753
	0.24	2.807150	2.16846	90.1726	0.005488980	5.48898
	0.30	3.964970	1.98801	89.1339	0.007025890	7.02589
	0.34	4.895900	1.87406	85.5127	0.007845970	7.84597
	0.40	1.402380	1.73311	36.718	0.000892422	0.892422
	0.45	0.191332	1.66713	45.3088	0.000144524	0.144524
	0.50	0.0281717	1.63904	54.2045	2.5028×10^{-5}	0.0250287
	0.52	0.0202431	1.63612	57.3880	1.9007×10^{-5}	0.019007
	0.57	0.0106039	1.63694	78.5582	1.3636×10^{-5}	0.0136361
	0.60	0.00902653	1.63896	81.3945	1.2041×10^{-5}	0.0120416

Qualitative study of Indium Gallium Nitride (InGaN) – based solar cell.
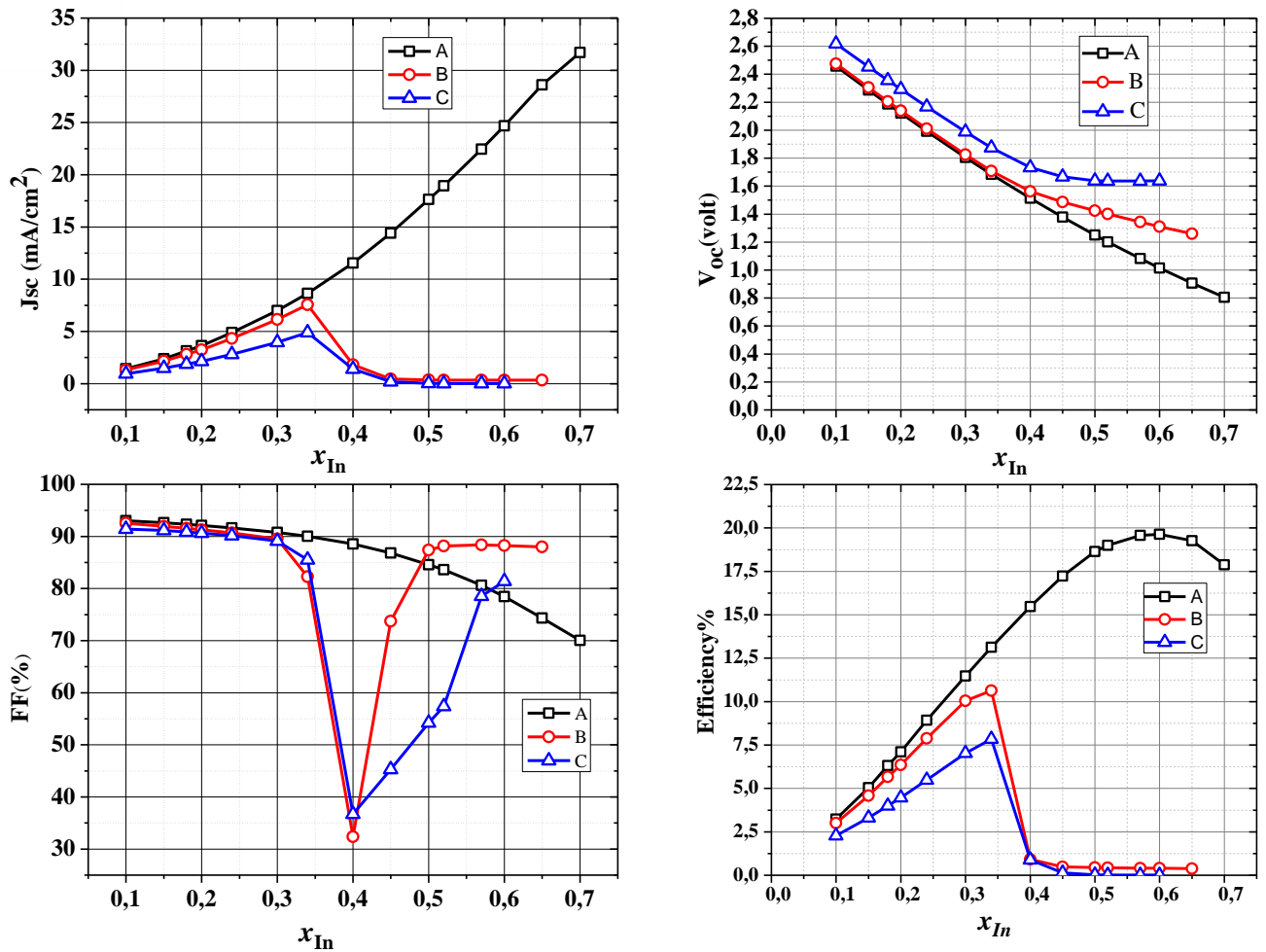
Figure IV. 14: Solar cell output parameters vs Indium concetraction (x_{IN}) for structures A, B, and C : a) Short circuit current, b) Open circuit voltage, c) Fill factor and d) Conversion efficiency .

Somes remarks can be notified from figure IV.14:

❖   The more x_{In} increases, the J_{SC} of the cell A increases until reaching a value of 31.6987 mA/cm² at $x_{In} = 0.7$, however in cells B and C, J_{SC} reaches, respectively, values of 7.5623 mA/cm² and 4.8959 mA/cm² at $x_{In} = 0.34$,and then begins to decrease. The cell A presents the ideal case, which provides the highest current. The limitations from GaN/InGaN interfaces in cells B and C, and from GaN/substrate discontinuity in cell C, reduce the current to a more realist behavior with optimum values at $x_{In} = 0.34$ corresponding to InGaN band gap of (2.1981).

❖ More we increase x_{In}, the V_{OC} decreases in all structures A, B, and C, because increasing the molar fraction of in means the reduction of the InGaN band gap, which leads to Voc diminution.

❖ As x_{In} increases, the fill factor FF decreases in the three structures with the exception that it reaches a minimum value around 32%-35% for the cells B and C, and then it begin to increase.

❖ The conversion efficiency increases with increasing indium concentration x_{In} until it reaches an optimal value of 19.62 % at $x_{In} = 0.6$ which corresponds to InGaN band gap of (1.4868)for the ieal case presented by the cell A. Taking into account the GaN/InGaN and GaN/substrate interface effect lead to more realist conversion efficiency which reaches for cell C an optimal value of 7.84% at $x_{In} = 0.34$ corresponding to InGaN band gap of (2.1981). We notify that 7.84% is in the best efficiency range obtained experimentally [65].

IV.3.1 Effect of defects

We observed from experimental measurements that the lifetime of $InGaN$ changes within the range $[10^{-9} - 10^{-6}\ sec]$ [42]. Therefore, the effect of defects can be studied by changing the lifetime values of electrons (τ_n) and holes (τ_p) within the range obtained experimentally [42, 63]. This is done by giving τ_n and τ_p the same values listed in Table IV .3 for the cell C optimized with $x_{In} = 0.34$. When activating the SRH model and inserting τ_n and τ_p values, Silvaco uses the simplest model of defects, which is presented, by single recombination center level in the middle of the band gap.

An increase of τ_n and τ_p values means a decrease in the defects concentration $N_R\ (cm^{-3})$ following equations IV.9-IV.11:

$$\tau_n = \frac{1}{C_n N_R} \qquad \text{(IV.9)}$$

$$\tau_p = \frac{1}{C_p N_R} \qquad \text{(IV.10)}$$

Where $C_P\ and\ C_n$ hole and electron are capture coefficients respectively $(cm^3 . sec^{-1})$.

The value of N_R is then deduced:

$$N_R = \frac{1}{C_n \tau_n} \qquad \text{(IV.11)}$$

The value of C_n can be calculated from Silvaco manuel which give $\tau_n = 10^{-7} sec$ for $N_R = 5 \times 10^{16} cm^{-3}$ [43] then :

$$C_n = \frac{1}{\tau_n N_R} = \frac{1}{10^{-7} \times 5 \times 10^{16}} = 2 \times 10^{-10} \ cm^3 . sec^{-1} .$$

N_R Corresponding to $\tau_n = 10^{-9} sec$ be then:

$$N_R = \frac{1}{2 \times 10^{-10} \times 10^{-9}} = 5 \times 10^{18} cm^{-3}.$$

Table IV. 3: Lifetime effect on the output parameters ($J_{SC}, V_{OC}, FF, P_{max}, and\ \eta$) of the cell C optimized with $x_{In} = 0.34$.

Cell C x_{In}=0.34		J_{sc} (mA/cm^2)	V_{oc} (Volt)	FF (%)	P_m (Watt/cm^2)	η (%)
τ_n(sec) $N_R (cm^{-3})$	1×10^{-9} 5×10^{18}	4.89565	1.57979	81.8165	0.00632777	6.32777
	5×10^{-9} 1×10^{18}	4.89585	1.65288	82.7531	0.00669659	6.69659
	1×10^{-8} 5×10^{17}	4.89588	1.68361	83.1373	0.0068528	6.85280
	5×10^{-8} 1×10^{17}	4.89590	1.75283	84.0105	0.00720951	7.20951
	1×10^{-7} 5×10^{16}	4.89590	1.78165	84.3804	0.00736032	7.36032
	5×10^{-7} 1×10^{16}	4.89590	1.84648	85.2051	0.0077027	7.70270
	1×10^{-6} 5×10^{15}	4.89590	1.87406	85.5127	0.00784597	7.84597
	5×10^{-6} 1×10^{15}	4.89590	1.94078	85.9674	0.00816851	8.16851

Figures IV.15- IV.18 show the lifetime (and the correspondingN_R) effects on the output parameters ($J_{SC}, V_{OC}, FF, and\ \eta$) of the cell C optimized with $x_{In} = 0.34$.
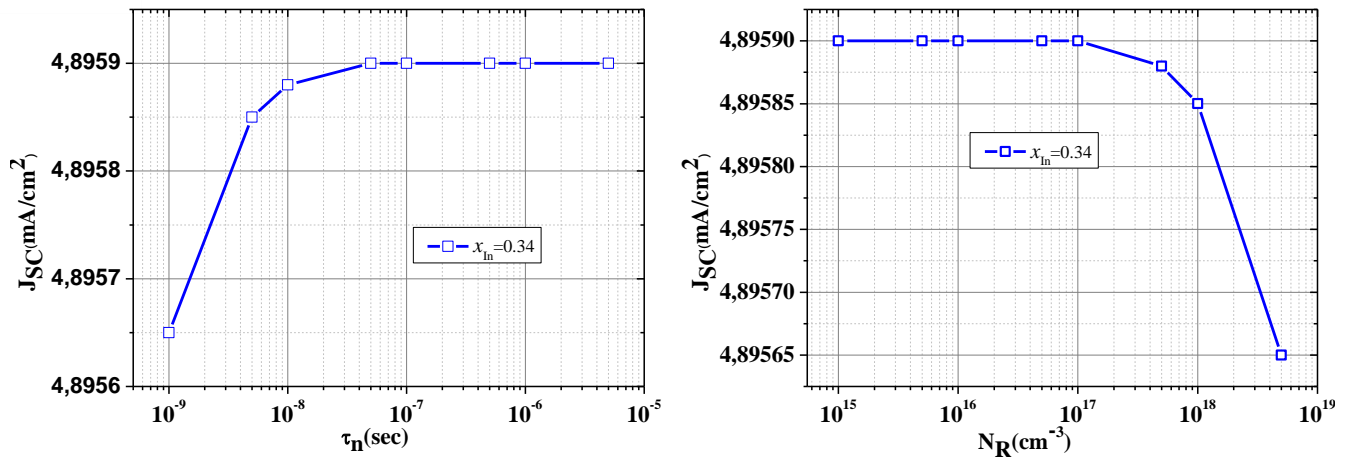
Figure IV. 15: Lifetime (and the corresponding N_R) effects on the J_{SC} of the cell C optimized with $x_{In} = 0.34$.

❖ J_{SC} Shows a slight increase as the lifetime τ_n increases corresponding to a defect concentration decrease.

❖ $\tau_n > 5 \times 10^{-8}s$ The current density J_{SC} becomes insensitive to further τ_n increase.
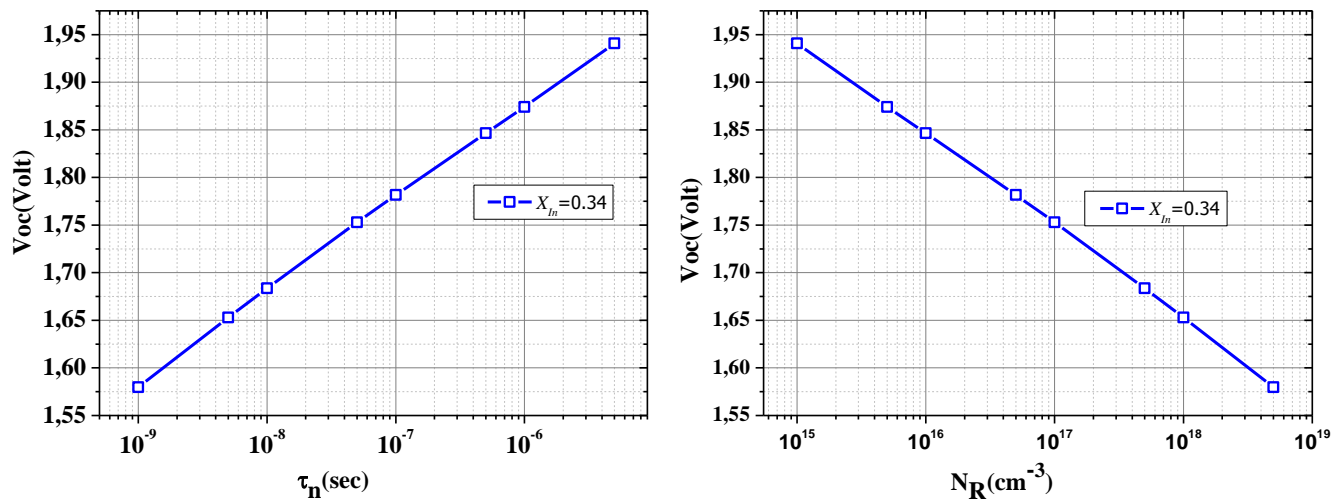
Figure IV. 16: Lifetime (and the corresponding N_R) effects on the V_{oc} of the cell C optimized with $x_{In} = 0.34$.

The V_{OC} however shows a discernible dependency on τ_n (and its corresponding N_R). The more we increase τ_n the greater is the V_{OC}, and this can be explained via the diffusion length L. Following equation IV.12, τ_n increase leads to diffusion length L increase:

$$L = \sqrt{D\tau_n} \tag{IV.12}$$

Where D the carrier diffusivity.

In addition, L increase leads to the saturation current J_0 decrease following equation IV.13:

$$J_0 = q.n_i^2 \left(\frac{D_n}{L_D N_A} + \frac{D_P}{L_P N_D}\right) \tag{IV.13}$$

Decrease of J_0 leads to the increased V_{OC} following the equation IV.3:

$$V_{OC} = \frac{k_\beta T}{q} ln \left(\frac{J_{SC}}{J_0} + 1\right) \tag{IV.14}$$

We can say that the τ_n increase leads to an increase in L and hence a decrease in J_0 and this leads to an increase in V_{OC} .
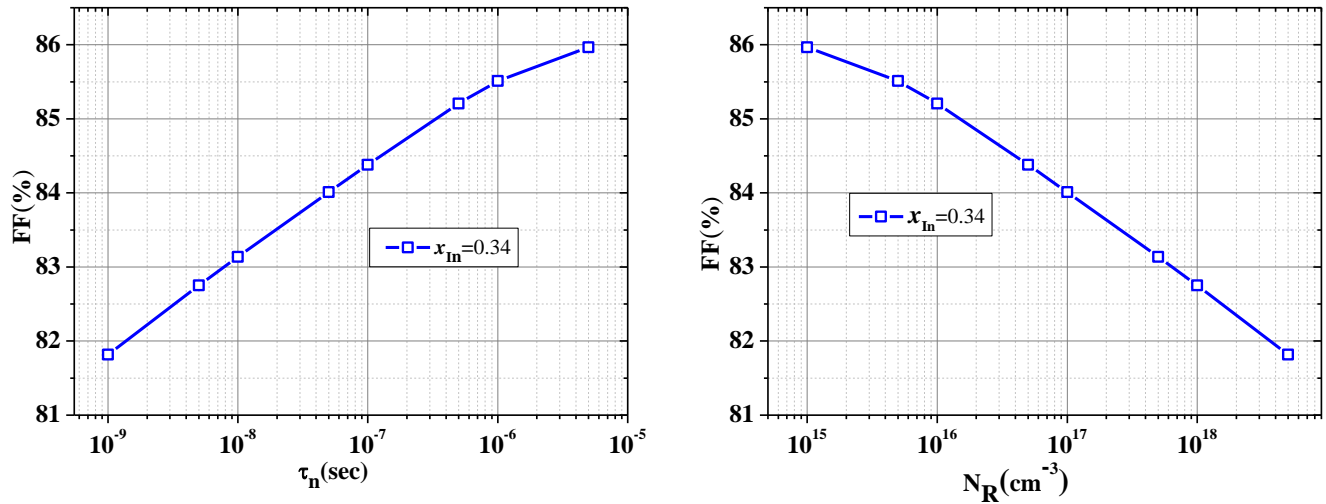
Figure IV. 17: Lifetime (and the corresponding N_R) effects on the FF of the cell C optimized with $x_{In} = 0.34$.

It is clear that a lifetime τ_n increase (which corresponds to N_R decrease) will enhance remarkably the fill factor FF.
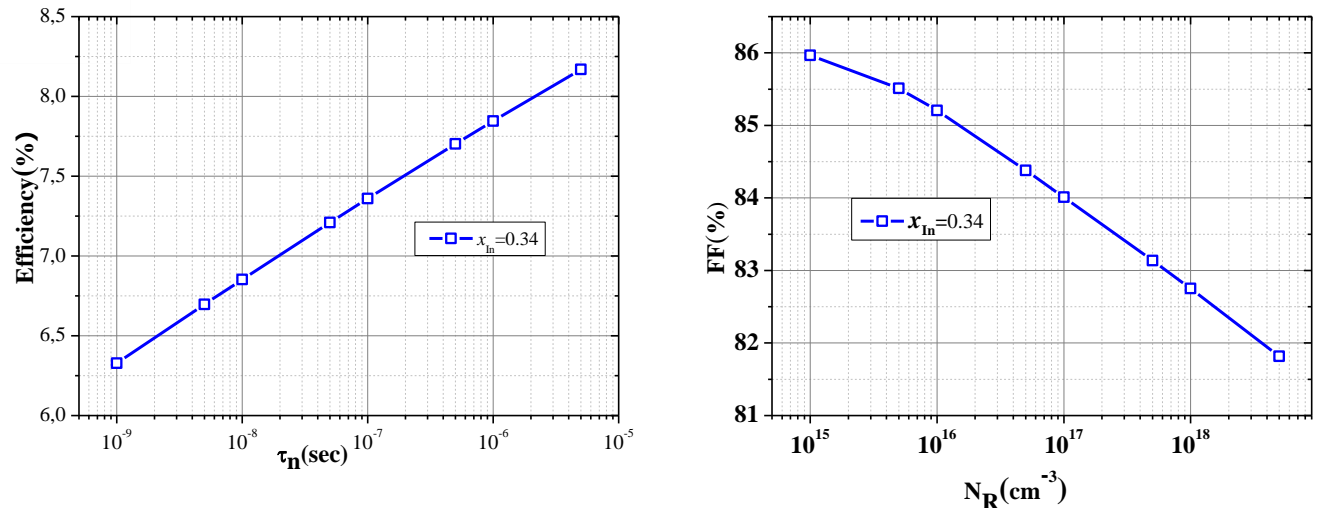
Figure IV. 18: Lifetime (and the corresponding N_R) effects on the conversion efficiency of the cell C optimized with $x_{In} = 0.34$.

The considerable improvement of V_{OC} and FF as the lifetime τ_n increases (or the N_R decreases) will lead to a considerable improvement of the conversion efficiency as shown in figure IV.18.

IV.3.2 Effect of $P - GaN$ layer thickness

The effect of $P - GaN$ layer thickness on solar cell output parameters of the PIN GaN/InGaN double heterojunction solar cell (cell C) is shown in Table IV.4 and on Figure IV.20. The $P - GaN$ layer thickness is varied from 50 to 270 nm.

Qualitative study of Indium Gallium Nitride (InGaN) – based solar cell.

Table IV. 4: $P - GaN$ layer thickness effect on the output parameters of the cell C optimized with $x_{In} = 0.34$.

Cell C x_{In}=0.34	$P - GaN$ thickness (nm)	J_{sc} (mA/cm^2)	V_{oc} (Volt)	FF (%)	P_m (Watt/cm^2)	η (%)
	50	4.89929	1.87344	80.2110	0.00736219	7.36219
	60	4.89930	1.87354	82.5956	0.00758148	7.58148
	70	4.89919	1.87364	83.6980	0.00768291	7.68291
	80	4.89892	1.87372	84.3130	0.00773926	7.73926
	90	4.89855	1.87380	84.7100	0.00777545	7.77545
	100	4.89806	1.87388	85.0015	0.00780176	7.80176
	110	4.89746	1.87394	85.2096	0.00782015	7.82015
	120	4.89675	1.87400	85.3708	0.00783406	7.83406
	130	4.89590	1.87406	85.5127	0.007845970	7.84597
	140	4.89494	1.8741	85.6241	0.00785482	7.85482
	150	4.89384	1.87414	85.7141	0.00786148	7.86148
	160	4.89262	1.87418	85.7888	0.00786653	7.86653
	170	4.89126	1.87421	85.8511	0.00787018	7.87018
	180	4.88978	1.87423	85.9137	0.00787362	7.87362
	190	4.88816	1.87425	85.9703	0.00787628	7.87628
	200	4.88640	1.87427	86.0195	0.00787804	7.87804
	210	4.88452	1.87428	86.0628	0.00787901	7.87901
	220	4.88251	1.87429	86.1014	0.00787935	7.87935
	230	4.88037	1.87429	86.1359	0.00787905	7.87905
	240	4.87810	1.87429	86.1668	0.00787821	7.87821
	250	4.87571	1.87429	86.1949	0.00787692	7.87692
	260	4.87319	1.87428	86.2204	0.00787513	7.87513
	270	4.87056	1.87427	86.2435	0.00787295	7.87295
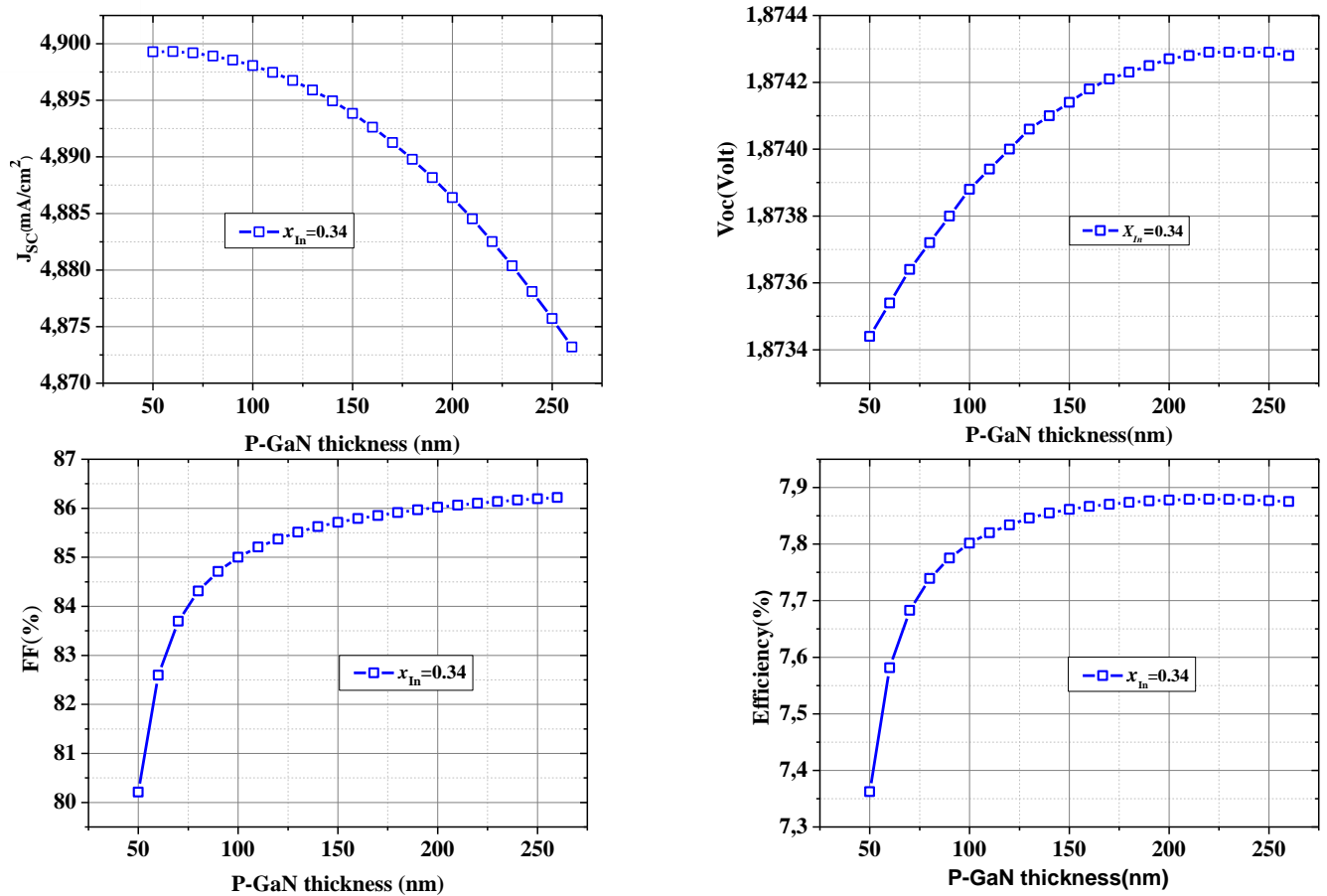
Figure IV. 19: Solar cell output parameters vs $P - GaN$ thickness for cell C: a)J_{sc}, b)V_{oc}, c) FF and d) Efficiency.

A slight decrease can be notified in the short circuit current density J_{sc} as the $P - GaN$ layer thickness increases, while the Voc shows a slight increase. The FF and efficiency show however a discernible improvement.

IV.3.3 Effect of $I - InGaN$ layer thickness

The effect of $I - InGaN$ layer thickness on solar cell output parameters of the PIN GaN/InGaN double heterojunction solar cell (cell C) is shown in Table IV.5 and on Figure IV.20. The $I - InGaN$ layer thickness is varied from 50 to 850 nm.

Table IV. 5: $I - InGaN$ layer thickness effect on the output parameters of the cell C optimized with $x_{In} = 0.34$.

Cell C x_{In}=0.34	$I - InGaN$ thickness (nm)	J_{sc} (mA/cm^2)	V_{oc} (Volt)	FF (%)	P_m (Watt/cm^2)	η (%)
	50	2.67298	1.90847	87.1017	0.00444332	4.44332
	100	4.20240	1.88417	86.3573	0.00683780	6.83780
	150	5.28845	1.86835	84.9033	0.00838902	8.38902
	200	6.08195	1.85627	83.309	0.00940537	9.40537
	250	6.67563	1.84648	81.7091	0.01007180	10.0718
	300	7.12889	1.83821	80.2425	0.01051530	10.5153
	350	7.48114	1.83102	78.9984	0.01082130	10.8213
	400	7.75930	1.82459	77.9811	0.01104020	11.0402
	450	7.98217	1.81891	77.1342	0.01119900	11.1990
	500	8.16313	1.81366	76.4343	0.01131620	11.3162
	550	8.31183	1.80894	75.8427	0.01140340	11.4034
	600	8.43542	1.80449	75.3487	0.01146930	11.4693
	650	8.53921	1.80047	74.9191	0.0115185	11.5185
	700	8.62719	1.79661	74.5486	0.0115548	11.5548
	750	8.70246	1.79304	74.2239	0.0115818	11.5818
	800	8.76735	1.78975	73.9368	0.0116017	11.6017
	850	8.82374	1.78652	73.6885	0.0116161	11.6161
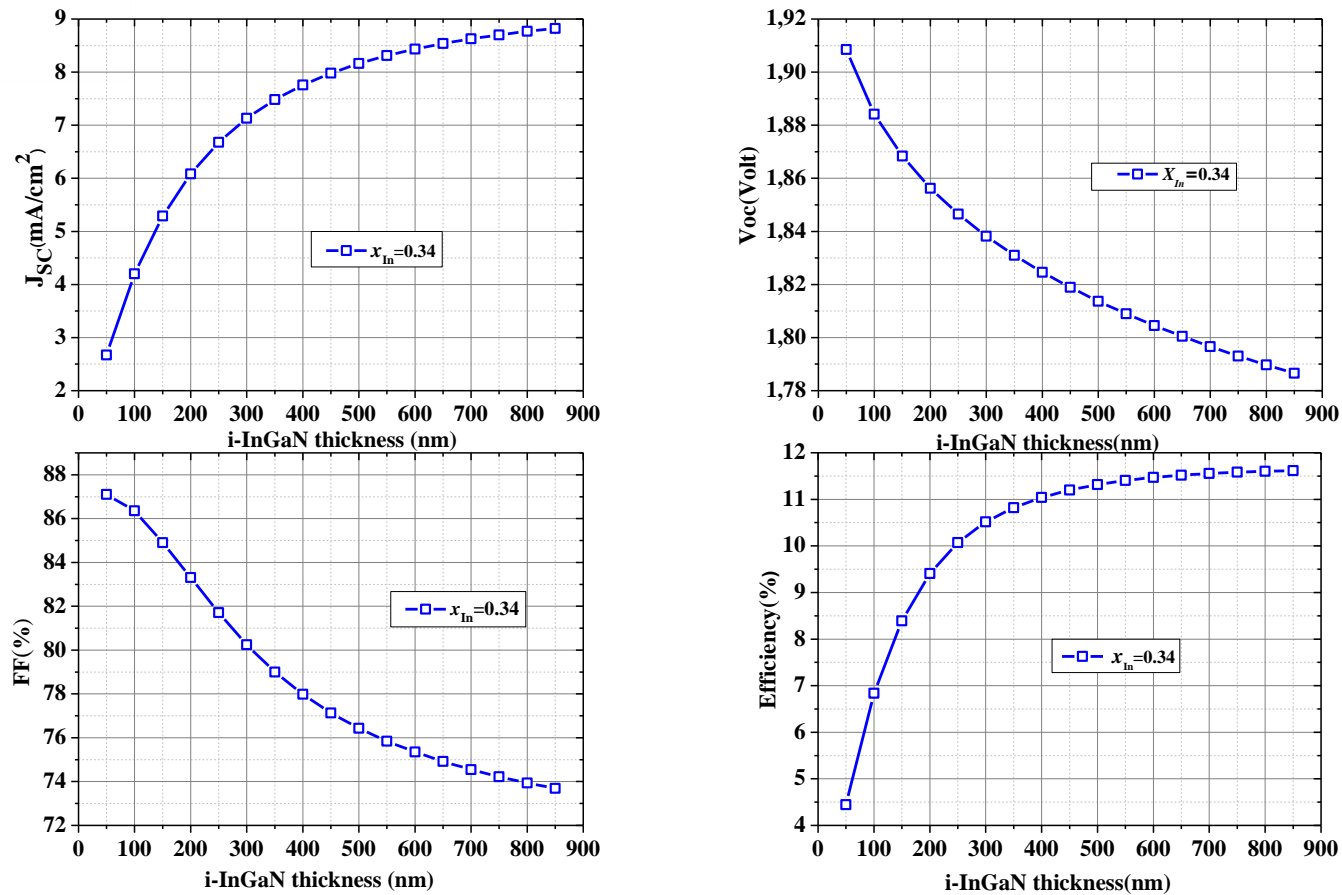
Figure IV. 20: Solar cell output parameters vs $I - InGaN$ thickness for cell C: a)J_{sc}, b)V_{oc}, c) FF and d) Efficiency.

❖ The J_{SC} increases as the $I - InGaN$ layer thickness increases and this can be explained by the photons, which get longer path for absorption, and unabsorbed lower energy photons from $p - GaN$ layer get absorbed in this region. Photon absorption is also supported by higher absorption coefficient of $InGaN$ material.

❖ The decrease in V_{OC} value as $I - InGaN$ layer increases by the fact that higher thickness generates more carriers and recombination, resulting in decreased open circuit voltage.

❖ The fill factor FF starts decreasing with respect to increased $I - InGaN$ thickness because the series resistance increases with increasing $I - InGaN$ thickness.

❖ The efficiency η increases as the $I - InGaN$ layer thickness increases and this can be explained by the fact that efficiency η follows the current density J_{SC} because the latter is the predominant and directly influencing factor.

IV.4 Conclusion

In this last chapter, we studied three InGaN-based PIN solar cell with the following structures: structure A which is a single InGaN homojunction, structure B which is GaN/InGaN heterojunction and structure C, which is a GaN/InGaN double heterojunction with GaN buffer layer on sapphire substrate. The three cells were investigated under solar radiation (AM1.5) and along with a wide energy range (by changing the molar fraction of indium x_{In}). The study was carried out using the Silvaco-Atlas software simulator. The latter allowed us to calculate the electric characteristics of the cell as the current density -voltage (J-V), and the power- voltage (P-V) characteristics, and the photovoltaic parameters related to these characteristics such as the short-circuit current density (Jsc), the open-circuit voltage (Voc); the maximum power ($Pmax$) delivered by the cell, the fill factor (FF), and the conversion efficiency (η). The largest efficiency is provided by the single homojunction solar cell (structure A) which gave 19.62% with ($In_{0.60}Ga_{0.40}N$) alloy. The better efficiency reached by the GaN/InGaN heterojunction solar cell (structure B) is 10.63% with ($In_{0.34}Ga_{0.66}N$) alloy. The GaN/InGaN double heterojunction (structure C) gave an optimal efficiency of 7.84% with ($In_{0.34}Ga_{0.66}N$) alloy. Further improvement of the structure C efficiency was achieved by the lifetime τ_n effect, which gave an optimal efficiency of 8.16%, by the $P - GaN$ layer thickness effect, which gave an optimal efficiency of 7.87%, and by the $I - InGaN$ layer thickness effect, which gave an optimal efficiency of 11.61%.

General conclusion

General conclusion

$InGaN$ alloy semiconductor materials have the potential to make a major breakthrough in the photovoltaic industry. Indeed these materials possess unique characteristics to achieve solar cells with very high efficiency of conversion and low cost: very high absorption coefficient across the spectrum solar energy, high mobilities, relatively low effective masses, an electronic gap which scans the entire visible spectrum, from the near infrared (InN gap = 0.77 eV) to ultraviolet (GaN gap = 3.4 eV), very high resistance to radiation and other extreme conditions. Despite this, $InGaN$-based cells really did not reach the expected efficiency due to manufacturing, design and other problems.

In this work, we studied three InGaN-based PIN solar cell with the following structures: structure A which is a single InGaN homojunction, structure B which is GaN/InGaN heterojunction and structure C, which is a GaN/InGaN double heterojunction with GaN buffer layer on sapphire substrate. The three cells were investigated under solar radiation (AM1.5) and along with a wide energy range (by changing the molar fraction of indium x_{In}). The study was carried out using the Silvaco-Atlas software simulator. The latter allowed us to calculate the electric characteristics of the cell as the current density -voltage (J-V), and the power- voltage (P-V) characteristics, and the photovoltaic parameters related to these characteristics such as the short-circuit current density (Jsc), the open-circuit voltage (Voc); the maximum power ($Pmax$) delivered by the cell, the fill factor (FF), and the conversion efficiency (η). The largest efficiency is provided by the single homojunction solar cell (structure A) which gave 19.62% with ($In_{0.60}Ga_{0.40}N$) alloy. The better efficiency reached by the GaN/InGaN heterojunction solar cell (structure B) is 10.63% with ($In_{0.34}Ga_{0.66}N$) alloy. The GaN/InGaN double heterojunction (structure C) gave an optimal efficiency of 7.84% with ($In_{0.34}Ga_{0.66}N$) alloy. Further improvement of the structure C efficiency was achieved by the lifetime τ_n effect, which gave an optimal efficiency of 8.16%, by the $P - GaN$ layer thickness effect, which gave an optimal efficiency of 7.87%, and by the $I - InGaN$ layer thickness effect, which gave an optimal efficiency of 11.61%.

REFERENCES

[1]   A. Mahfoud, "Modélisation des cellules solaires tandem à couches minces et à haut rendement," 2018.

[2]   *https://venturesolar.com/the-importance-of-solar-energy/*.

[3]   M. Grätzel, "Photoelectrochemical cells," *nature,* vol. 414, p. 338, 2001.

[4]   A. G. Bhuiyan, K. Sugita, A. Hashimoto, and A. Yamamoto, "InGaN solar cells: present state of the art and important challenges," *IEEE Journal of photovoltaics,* vol. 2, pp. 276-293, 2012.

[5]   J. Tang, "From Silicon to Germanium Nanowires: growth processes and solar cell structures," Université Paris-Saclay, 2017.

[6]   A. M. Bagher, M. M. A. Vahid, and M. Mohsen, "Types of solar cells and application," *American Journal of optics and Photonics,* vol. 3, pp. 94-113, 2015.

[7]   R. K. Pachauri, M. R. Allen, V. R. Barros, J. Broome, W. Cramer, R. Christ, J. A. Church, L. Clarke, Q. Dahe, and P. Dasgupta, *Climate change 2014: synthesis report. Contribution of Working Groups I, II and III to the fifth assessment report of the Intergovernmental Panel on Climate Change*: IPCC, 2014.

[8]   L. M. Fraas and L. D. Partain, *Solar cells and their applications* vol. 236: John Wiley & Sons, 2010.

[9]   L. M. Fraas, "History of solar cell development," in *Low-Cost Solar Electric Power*, ed: Springer, 2014, pp. 1-12.

[10]   A. Piebalgs and J. Potocnik, "Photovoltaic Solar Energy Development and Current Research," *European Communities, ISBN 978-92-79-10644,* vol. 6, 2009.

[11]   A. BENMIR, "Simulation d'une cellule solaire photovoltaïque en couche mince à hétérojonction: CdS/CIGS et CdS/CZTS."

[12]   *https://www.pveducation.org/pvcdrom/welcome-to-pvcdrom/solar-cell-operation*.

[13]   D. Vasileska and G. Klimeck, "Solar Cells Operation and Modeling," 2010.

[14]   N. Oleksiy, "Simulation, fabrication et analyse de cellules photovoltaïques à contacts arrières interdigités," *Institut national des sciences appliquée de Lyon,* 2005.

[15]   S. O. Kasap, *Principles of electronic materials and devices* vol. 2: McGraw-Hill New York, 2006.

[16]   C. Algora, E. Ortiz, I. Rey-Stolle, V. Díaz, R. Peña, V. M. Andreev, V. P. Khvostikov, and V. D. Rumyantsev, "A GaAs solar cell with an efficiency of 26.2% at 1000 suns and 25.0% at 2000 suns," *IEEE Transactions on Electron Devices,* vol. 48, pp. 840-844, 2001.

[17]   A. Blakers, N. Zin, K. R. McIntosh, and K. Fong, "High efficiency silicon solar cells," *Energy Procedia,* vol. 33, pp. 1-10, 2013.

[18]   M. Powalla, S. Paetel, D. Hariskos, R. Wuerz, F. Kessler, P. Lechner, W. Wischmann, and T. M. Friedlmeier, "Advances in cost-efficient thin-film photovoltaics based on Cu (In, Ga) Se2," *Engineering,* vol. 3, pp. 445-451, 2017.

[19]   S. Moon, K. Kim, Y. Kim, J. Heo, and J. Lee, "Highly efficient single-junction GaAs thin-film solar cell on flexible substrate," *Scientific reports,* vol. 6, p. 30107, 2016.

[20]   S. Nakamura, M. Senoh, and T. Mukai, "Highly p-typed Mg-doped GaN films grown with GaN buffer layers," *Japanese journal of applied physics,* vol. 30, p. L1708, 1991.

[21]   C. Himwas, "III-Nitride nanostructures for UV emitters," Université Grenoble Alpes, 2015.

[22]   L. Hsu and W. Walukiewicz, "Modeling of InGaN/Si tandem solar cells," *Journal of Applied Physics,* vol. 104, p. 024507, 2008.

[23] M. Higashiwaki, T. Inushima, and T. Matsui, "Control of electron density in InN by Si doping and optical properties of Si-doped InN," *physica status solidi (b),* vol. 240, pp. 417-420, 2003.

[24] D. McLaughlin, "Optical Characterization of Indium Gallium Nitride for Application in High-Efficiency Solar Photovoltaic Cells," 2011.

[25] M. Anani, H. Abid, Z. Chama, C. Mathieu, A. Sayede, and B. Khelifa, "InxGa1− xN refractive index calculations," *Microelectronics Journal,* vol. 38, pp. 262-266, 2007.

[26] Q. A. H. Al-Naser, H. W. Hilou, and A. F. Abdulkader, "The last development in III-V multi-junction solar cells," in *2009 ISECS International Colloquium on Computing, Communication, Control, and Management*, 2009, pp. 373-378.

[27] V. Y. Davydov, A. Klochikhin, V. V. Emtsev, D. Kurdyukov, S. Ivanov, V. Vekshin, F. Bechstedt, J. Furthmüller, J. Aderhold, and J. Graul, "Band gap of hexagonal InN and InGaN alloys," *physica status solidi (b),* vol. 234, pp. 787-795, 2002.

[28] Y. Sato and S. Sato, "Growth and some properties of Inx Ga1− x N thin films by reactive evaporation," *Thin Solid Films,* vol. 261, pp. 87-89, 1995.

[29] O. Jani, I. Ferguson, C. Honsberg, and S. Kurtz, "Design and characterization of Ga N∕ In Ga N solar cells," *Applied Physics Letters,* vol. 91, p. 132117, 2007.

[30] Y. Nanishi, Y. Saito, and T. Yamaguchi, "RF-molecular beam epitaxy growth and properties of InN and related alloys," *Japanese journal of applied physics,* vol. 42, p. 2549, 2003.

[31] R. Dahal, B. Pantha, J. Li, J. Lin, and H. Jiang, "InGaN/GaN multiple quantum well solar cells with long operating wavelengths," *Applied Physics Letters,* vol. 94, p. 063505, 2009.

[32] M. Yamaguchi, T. Takamoto, and K. Araki, "Super high-efficiency multi-junction and concentrator solar cells," *Solar energy materials and solar cells,* vol. 90, pp. 3068-3077, 2006.

[33] F. Yam and Z. Hassan, "InGaN: An overview of the growth kinetics, physical properties and emission mechanisms," *Superlattices and Microstructures,* vol. 43, pp. 1-23, 2008.

[34] T. Takeuchi, H. Takeuchi, S. Sota, H. Sakai, H. Amano, and I. Akasaki, "Optical properties of strained AlGaN and GaInN on GaN," *Japanese journal of applied physics,* vol. 36, p. L177, 1997.

[35] P. Schley, R. Goldhahn, A. Winzer, G. Gobsch, V. Cimalla, O. Ambacher, H. Lu, W. Schaff, M. Kurouchi, and Y. Nanishi, "Dielectric function and Van Hove singularities for In-rich In x Ga 1− x N alloys: Comparison of N-and metal-face materials," *Physical Review B,* vol. 75, p. 205204, 2007.

[36] J. Wu, W. Walukiewicz, K. M. Yu, J. Ager III, E. Haller, H. Lu, and W. J. Schaff, "Small band gap bowing in In 1− x Ga x N alloys," *Applied Physics Letters,* vol. 80, pp. 4741-4743, 2002.

[37] S. Nakamura, "Growth of InxGa (1− x) N compound semiconductors and high-power InGaN/AlGaN double heterostructure violet-light-emitting diodes," *Microelectronics Journal,* vol. 25, pp. 651-659, 1994.

[38] S. Pereira, M. Correia, T. Monteiro, E. Pereira, E. Alves, A. Sequeira, and N. Franco, "Compositional dependence of the strain-free optical band gap in In x Ga 1− x N layers," *Applied Physics Letters,* vol. 78, pp. 2137-2139, 2001.

[39] W. Shan, W. Walukiewicz, E. Haller, B. Little, J. Song, M. McCluskey, N. Johnson, Z. Feng, M. Schurman, and R. Stall, "Optical properties of In x Ga 1− x N alloys grown by metalorganic chemical vapor deposition," *Journal of Applied Physics,* vol. 84, pp. 4452-4458, 1998.

[40] J. W. A. G.F.Brown, W.Walukiewicz,J.Wu,Sol., "EnergyMater.Sol.Cells94," pp. 478– 483., 2010.

[41] R. Belghouthi, S. Taamalli, F. Echouchene, H. Mejri, and H. Belmabrouk, "Modeling of polarization charge in N-face InGaN/GaN MQW solar cells," *Materials Science in semiconductor Processing,* vol. 40, pp. 424-428, 2015.

[42] G. Brown, J. Ager III, W. Walukiewicz, and J. Wu, "Finite element simulations of compositionally graded InGaN solar cells," *Solar energy materials and solar cells,* vol. 94, pp. 478-483, 2010.

[43] P. Henry, *Atlas User's Manual DEVICE SIMULATION SOFTWARE*, 2015.

[44] M. Leszczynski, R. Czernecki, S. Krukowski, M. Krysko, G. Targowski, P. Prystawko, J. Plesiewicz, P. Perlin, and T. Suski, "Indium incorporation into InGaN and InAlN layers grown by metalorganic vapor phase epitaxy," *Journal of Crystal Growth,* vol. 318, pp. 496-499, 2011.

[45] M. Gartner, C. Kruse, M. Modreanu, A. Tausendfreund, C. Roder, and D. Hommel, "Optical characterization of InxGa1− xN alloys," *Applied surface science,* vol. 253, pp. 254-257, 2006.

[46] C. Parker, J. Roberts, S. Bedair, M. Reed, S. Liu, and N. El-Masry, "Determination of the critical layer thickness in the InGaN/GaN heterostructures," *Applied Physics Letters,* vol. 75, pp. 2776-2778, 1999.

[47] V. Gorge, "Caractérisations de matériaux et tests de composants des cellules solaires à base des nitrures des éléments III-V," Paris 11, 2012.

[48] K. Iwata, H. Asahi, K. Asami, R. Kuroiwa, and S.-i. Gonda, "Gas source molecular beam epitaxy growth of GaN on C-, A-, R-and M-plane sapphire and silica glass substrates," *Japanese journal of applied physics,* vol. 36, p. L661, 1997.

[49] S. O. Kasap, *Principles of electrical engineering materials and devices*: McGraw-Hill Companies, 2000.

[50] M. Adaika, "Effet des défauts sur le fonctionnement d'un transistor couche mince (TFT): Comparaison entre un TFT en a-Si: H et un TFT en a-IGZO par SILVACO ATLAS," 2017.

[51] N. Benadla, "Optimisation des émetteurs sélectifs et passivables des cellules solaires conventionnelles à base de mc_si."

[52] P. Michalopoulos, "A novel approach for the development and optimization of state-of-the-art photovoltaic devices using Silvaco," NAVAL POSTGRADUATE SCHOOL MONTEREY CA2002.

[53] W. DIB, "Modélisation des structures photovoltaïques: Aspects fondamentaux et appliqués," 2011.

[54] *https://www.silvaco.com/*.

[55] B. Garcia Jr, "Indium gallium nitride multijunction solar cell simulation using silvaco atlas," NAVAL POSTGRADUATE SCHOOL MONTEREY CA2007.

[56] K. Fotis, "Modeling and simulation of a dual-junction CIGS solar cell using Silvaco ATLAS," NAVAL POSTGRADUATE SCHOOL MONTEREY CA2012.

[57] *Atlas User's Manual: Device Simulation Software*, 2013.

[58] D. Schiavo, "Modeling Radiation Effects on a Triple Junction Solar Cell using Silvaco ATLAS," NAVAL POSTGRADUATE SCHOOL MONTEREY CA2012.

[59] S. Chala, "II-VI Design and investigate of تصوين و بحث الخلايا الشوسيت ذاث الطبقاث الرقيقت" II-VI thin film solar cells Conception et investigation des cellules solaires en couches minces II-VI," UNIVERSITE DE MOHAMED KHIDER BISKRA, 2017.

[60] R. Boumaraf, "Simulation de l'effet de la température et les défauts sur les caractéristiques électriques des diodes à base de GaAs," Université Mohamed Khider-Biskra, 2015.

[61] M. Nawaz and A. Ahmad, "A TCAD-based modeling of GaN/InGaN/Si solar cells," *Semiconductor Science and Technology,* vol. 27, p. 035019, 2012.

[62]   M. E. Levinshtein, S. L. Rumyantsev, and M. S. Shur, *Properties of Advanced Semiconductor Materials: GaN, AIN, InN, BN, SiC, SiGe*: John Wiley & Sons, 2001.

[63]   S. Lin, S. Zeng, X. Cai, J. Zhang, S. Wu, L. Sun, and B. Zhang, "Simulation of doping levels and deep levels in InGaN-based single-junction solar cell," *Journal of Materials Science,* vol. 47, pp. 4595-4603, 2012.

[64]   *http://www.ioffe.ru/SVA/NSM/Semicond/GaN/ebasic.htm*.

[65]   A. S. Kushwaha, P. Mahala, and C. Dhanavantri, "Optimization of p-GaN/InGaN/n-GaN double heterojunction pin solar cell for high efficiency: simulation approach," *International Journal of Photoenergy,* vol. 2014, 2014.

Abstract

In this work, we studied three $InGaN$-based PIN solar cell. The first one is a single $InGaN$ homojunction (structure A), the second one is a GaN/InGaN heterojunction (structure B) and the third one is a $GaN/InGaN$ double heterojunction with GaN buffer layer on sapphire substrate (structure C). The study was carried out using the Silvaco-Atlas software simulator. The largest efficiency was provided by the cell A which gave 19.62% with ($In_{0.60}Ga_{0.40}N$) alloy. The better efficiency reached by the cell B is 10.63% with ($In_{0.34}Ga_{0.66}N$) alloy. The cell C gave an optimal efficiency of 7.84% with ($In_{0.34}Ga_{0.66}N$) alloy. Further improvement of the cell C efficiency was achieved by the lifetime τ_n effect, which gave an optimal efficiency of 8.16%, by the $P - GaN$ layer thickness effect, which gave an optimal efficiency of 7.87%, and by the $I - InGaN$ layer thickness effect, which gave an optimal efficiency of 11.61%.

Key words: InGaN- solar cell- Efficiency -Simulation- Silvaco Atlas.

Résumé

Dans ce travail, nous avons étudié trois cellules solaires PIN basées sur $InGaN$. Le premier est une homojonction $InGaN$ unique (structure A), le deuxième est une hétérojonction GaN / InGaN (structure B) et le troisième est une hétérojonction double GaN / InGaN avec une couche tampon de GaN sur un substrat en saphir (structure C). L'étude a été réalisée à l'aide du simulateur logiciel Silvaco-Atlas. La plus grande efficacité a été fournie par la cellule A qui a donné 19,62% d'alliage ($In_{0.60}Ga_{0.40}N$) . La meilleure efficacité atteinte par la cellule B est de 10,63% avec l'alliage $In_{0.34}Ga_{0.66}N$) . La cellule C a donné un rendement optimal de 7,84% avec l'alliage ($In_{0.34}Ga_{0.66}N$) .L'efficacité de la cellule C a été améliorée grâce à l'effet de durée de vie τ_n qui donnait une efficacité optimale de 8,16%, à l'effet d'épaisseur de couche P-GaN qui donnait une efficacité optimale de 7,87% et à l'effet d'épaisseur de couche I-$InGaN$ qui une efficacité optimale de 11,61%.

Mots clés: $InGaN$ - cellule solaire - Efficacité – Simulation-Silvaco Atlas.

<div dir="rtl">

ملخص

في هذا العمل، درسنا ثلاث خلايا شمسية PIN تستند إلى $InGaN$ أول خلية هي homojunction $InGaN$(بنية A)، والثانية هي GaN / $InGaN$ heterojunction (بنية B) والثالثة هي double heterojunction GaN / $InGaN$ مع طبقة GaN عازلة على طبقة ياقوت (بنية C).

أجريت الدراسة باستخدام محاكي برمجيات Silvaco-Atlas. تم توفير أكبر كفاءة من قبل الخلية A التي أعطت 19.62 ٪ ($In_{0.60}Ga_{0.40}N$). أفضل كفاءة وصلت إليها الخلية B هي 10.63٪ ($In_{0.34}Ga_{0.66}N$). أعطت الخلية C كفاءة مثالية قدرها 7.84 ٪ ($In_{0.34}Ga_{0.66}N$) . تم تحقيق المزيد من التحسن في كفاءة الخلية C من خلال تأثير مدة الحياة τ_n والذي أعطى كفاءة مثالية بنسبة 8.16 ٪ ، وتأثير سماكة طبقة GaN -P الذي أعطى كفاءة مثالية قدرها 7.87 ٪ وتأثير سمك طبقة $InGaN$-I الذي أعطى كفاءة مثالية من 11.61 ٪.

الكلمات المفتاحية: $InGaN$-الخلية الشمسية- المردود -المحاكاة- سيلفاكوأطلس.

</div>